

Bayesian inferences on covariant density functionals from multimessenger astrophysical data: Nucleonic models

Jia-Jie Li,^{1,*} Yu Tian,¹ and Armen Sedrakian^{2,3,†}

¹*School of Physical Science and Technology, Southwest University, Chongqing 400715, China*

²*Frankfurt Institute for Advanced Studies, D-60438 Frankfurt am Main, Germany*

³*Institute of Theoretical Physics, University of Wrocław, 50-204 Wrocław, Poland*

(Dated: May 23, 2025)

Background: Bayesian inference frameworks incorporating multi-messenger astrophysical constraints have recently been applied to covariant density functional (CDF) models to constrain their parameters. Among these, frameworks utilizing CDFs with density-dependent meson-nucleon couplings furnishing the equation of state (EoS) of compact star (CS) matter have been explored. This class of CDF models has been extensively tested against various nuclear phenomena, providing a highly predictive description of CSs in terms of nuclear characteristics defined in the vicinity of nuclear saturation density and isospin symmetric limit.

Purpose: The aforementioned inference framework has not yet incorporated astrophysical objects with potentially extreme high masses or ultra-small radii among its constraints, leaving its flexibility and predictive power under such extreme parameters still unknown. We aim at exploring the capabilities of this framework to account for these additional data.

Method: We apply the Bayesian inference framework based on CDFs with density dependent couplings. The astrophysical data are expanded to include not only the latest multi-messenger constraints from NICER telescope and gravitational wave events but also the highest measured mass to date for the “black widow” pulsar PSR J0952-0607 and the mass-radius estimates for the ultra-compact, low-mass object HESS J1731-347. The significance of the individual impact of these two sources, as well as the broader picture that emerges from their combined influence, is examined by analyzing the posterior distributions of key CS properties, nuclear characteristics at saturation density, and their correlations.

Results: Our systematic Bayesian analysis, which incorporates the PSR J0952-0607 and/or HESS J1731-347 data alongside typical astrophysical constraints, indicates that our CDF models can support higher maximum masses for CSs, reaching up to $2.4\text{--}2.5 M_{\odot}$. However, achieving sufficient softening of the EoS in the low-density regime to accommodate the HESS J1731-347 data remains challenging. Nonetheless, we are able to impose tighter constraints on the parameter space of CDF models, ensuring consistency with current nuclear experimental and astrophysical data.

Conclusions: CDF models with density-dependent meson-nucleon couplings encompass a wide range of nuclear and astrophysical phenomena, providing a robust theoretical framework for interpreting compact objects. However, the predicted lower limit for the radii of low-mass stars is approximately 12 km, which stems from the restricted degrees of freedom in the isovector sector. These limitations can be addressed by extending CDF models to introduce more complex density dependence of the symmetry energy. Additionally, smaller radii may be achieved by allowing for a low-density deconfinement phase transition to quark matter.

I. INTRODUCTION

The systematic construction of dense matter equation of state (EoS) models and statistical inference of EoS parameters from data is an endeavor that has recently attracted significant attention. The Bayesian framework has been applied to models covering the range from fully physics agnostic non-parametric models [1–11] to microscopic models based on nuclear potentials [12–16] to density functional method-based models [17–32]. This effort has matured in the current era of multi-messenger astronomy with a large push to explore model-dependence in statistical inferences. The future thus lies in combining more and more sets of data of both types to understand nuclear and neutron star models better.

The main motivation of this work is to extend our previous study of covariant density functional (CDF, with linear meson-baryon couplings and density-dependent coupling constants) based Bayesian inference for compact stars (CSs) with well-

established astrophysical constraints [31] to those that including more extreme and less certain constraints. This provides a more complete exploration of the parameter space that admits the existence of very massive or ultra-compact stars. The astrophysical constraints for the sources that we considered in the present analysis are summarized in Fig. 1. We aim to assess the compatibility of the parameter space over which these models are defined with the recent multi-messenger observations of CSs. We stress that previous studies of this sort of CDF used simplified functions for density dependence of meson-baryon couplings [18, 19, 24, 28], which thus reduced the flexibility of the model.

The remainder of this introduction provides a detailed overview of current astrophysical constraints in Subsec. IA and a review of the current state of the art of the dense matter theories in Subsec. IB. Readers familiar with these topics can proceed directly to Sec. II which discusses the specific CDF model of dense matter used in our analysis. The Bayesian inference framework adopted in this work and underlying numerical methods are discussed in Sec. III. Our analysis is specific to the cases of the ultra-compact low-mass star HESS J1731-347 and the high-mass star PSR J0952-0607 in Sec. IV where we study the impact of these data on the overall picture

* jiajieli@swu.edu.cn

† sedrakian@fias.uni-frankfurt.de

that emerges once these are included in the inference analysis. Our conclusions and outlook are given in Sec. V.

A. Summary of astrophysical constraints

Significant advancements in astrophysical observations of CSs over the past decade have provided valuable constraints on dense matter theories. The first observation of gravitational wave (GW) event GW170817 from the inspiral of a binary neutron stars by the LIGO-Virgo Collaboration placed constraints on the dimensionless tidal deformability (TD) of this system, $\tilde{\Lambda}_{\text{GW170817}} \leq 720$ at 90% confidence interval (hereafter CI), and on the range of the component masses 1.17 – $1.60 M_{\odot}$ [33–35]. GW190425 is a highly significant gravitational wave signal, most likely originating from the merger of two neutron stars, making it the second such event ever observed. The TD parameter is constrained to $\tilde{\Lambda}_{\text{GW190425}} \leq 600$, with component masses being within the range 1.46 – $1.87 M_{\odot}$ [36]. Neutron Star Interior Composition Explorer Mission (NICER) has provided mass–radius estimates for four pulsars by observing X-ray emission from hot spots on the neutron stars’ surfaces. The first estimates for one of the most massive known neutron star PSR J0740+6620 [37, 38] was updated from a joint NICER and XMM-Newton analysis of the 2018-2022 dataset, refining the radius and mass to $12.49^{+1.28}_{-0.88}$ km and $2.073^{+0.069}_{-0.069} M_{\odot}$, respectively [39]. The updated analysis of the isolated pulsar PSR J0030+0451 revealed that it is a complex source to model, with solutions varying depending on the assumed model. Reference [40]

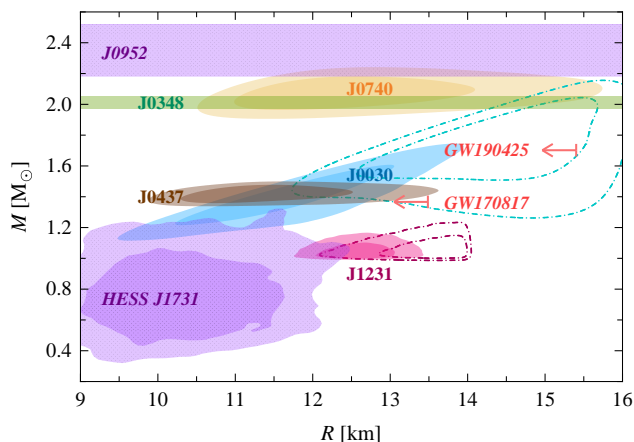


FIG. 1. The observational mass and/or radius estimates that represent the multimessenger astrophysical constraints adopted in this study. These ellipses correspond to the 68.3% and 95.4% CIs for the latest and updated NICER measurements of four pulsars, and the results for HESS J1731, and these horizontal bands correspond to the mass only measurements for two massive pulsars at 68.3% CI, all labeled in the figure. The NICER mass-radius estimates include the most recent measurement for PSR J0437, two estimates for J1231, the reanalysis of J0740, and two possible solutions for J0030. The radius upper limits obtained from two binary-neutron-star mergers are incorporated into the figure as well. Further details are provided in the text.

adopted the same models used in the initial studies [41, 42], and found compatible but slightly more stringent results $R = 13.11^{+1.30}_{-1.30}$ km and $M = 1.37^{+0.17}_{-0.17} M_{\odot}$. When XMM-Newton data are accounted for, the model that is more consistent with the magnetic field geometry inferred for the gamma-ray emission for this source inferred radius and mass of $R = 11.71^{+0.88}_{-0.83}$ km and $M = 1.40^{+0.13}_{-0.12} M_{\odot}$ (at 68.3% CI). The most complex model tested in Ref. [40], which is highly preferred by the Bayesian evidence, predicts $R = 14.438^{+0.883}_{-1.050}$ km and $M = 1.70^{+0.18}_{-0.19} M_{\odot}$. Recently, new NICER astrophysical constraints have been released for two pulsars — one canonical-mass $1.4 M_{\odot}$ star PSR J0437-4715 [43], and the one-solar-mass star PSR J1231-1411 [44]. For the nearest and brightest pulsar PSR J0437-4715, its first mass and radius are $M = 1.418^{+0.037}_{-0.037} M_{\odot}$ and $R = 11.36^{+0.95}_{-0.63}$ km, by using the 2017-2021 NICER X-ray spectral-timing data [43]. The inference results for PSR J1231-1411 exhibit a strong sensitivity to the choice of radius priors, with stable and well-converged outcomes achieved only under constrained radius priors. When the radius is restricted to agree with previous observational constraints and EoS analyses, the inferred values are $R = 12.60^{+0.31}_{-0.33}$ km and $M = 1.04^{+0.05}_{-0.03} M_{\odot}$ [44].

The mass range for neutron stars covered by the aforementioned data spans the range 1 – $2 M_{\odot}$. Correspondingly, the relevant range for densities spans 2 – $4 \rho_{\text{sat}}$, with $\rho_{\text{sat}} \simeq 0.16 \text{ fm}^{-3}$ being the nuclear saturation density. This opens an unprecedented opportunity to explore models of modern theories of dense matter subject to astrophysical constraints. For example, the impact of variations in the estimates for PSR J0030+0451 [40] on dense matter theories and CS properties have recently been assessed [10, 31, 45]. In addition, the X-ray observations of the temperature of the neutron star in the Cassiopeia A supernova remnant and modeling of its thermal evolution give insights into the possible superfluid properties of the core matter [46].

Determining the maximum mass of neutron stars is crucial for understanding stellar evolution, supernovae, and binary mergers, as well as their observational signatures. This value primarily depends on the EoS at high densities, $\rho > 4\rho_{\text{sat}}$. Most observed neutron stars rotate significantly more slowly than their theoretical Keplerian break-up limit (e.g. Ref [47] and references therein). As a result, mass measurements are commonly used to establish lower bounds on the maximum mass of cold, non-rotating neutron stars M_{max} , even though rapid rotation can support up to $\sim 20\%$ additional mass. The highest precisely and reliably measured massive mass belongs to pulsar PSR J0348+0432, with a mass estimate of $M = 2.01^{+0.04}_{-0.04} M_{\odot}$ (at 68.3% CI) [48]. The heavier pulsar, PSR J0740+6620, has a mass of $M = 2.08^{+0.07}_{-0.07} M_{\odot}$ [49, 50] and excludes all the EoS models which cannot reach this limit. At the same time the analysis of the kilonova AT2017gfo and GRB170817A [51, 52], associated with GW170817, have helped in designing theoretical models of the post-merger phase of GW170817 that placed an upper limit on the maximum mass $M_{\text{max}} \sim 2.3 M_{\odot}$ [53–58].

These mass limits have been further challenged by evidence suggesting the existence of even heavier compact objects. The “black widow” pulsar PSR J0952-0607, the second-

fastest known spinning CS with a rotation frequency of 707 Hz, was detected in the Milky Way with a mass estimate of $M = 2.35^{+0.17}_{-0.17} M_{\odot}$ (at 68.3% CI) [59], making it the most massive neutron star observed to date.

More recently, pulsar timing observations conducted with the Karoo Array Telescope (MeerKAT) revealed that the eccentric binary millisecond pulsar PSR J0514-4002E in the globular cluster NGC 1851 has a companion with a mass in the range of 2.09 - $2.71 M_{\odot}$ (at 95.4% CI) [60]. This mass falls within the so-called “mass gap” ($2.5 \lesssim M/M_{\odot} \lesssim 5$) between known neutron stars and black holes, suggesting either an exceptionally massive neutron star or a low-mass black hole.

Additionally, compact objects observed in GW events have been found within this mass gap. Examples include the lighter components of black hole-black hole or black hole-neutron star merger candidates, such as GW190814, where the secondary has a mass of $M_2 = 2.59^{+0.08}_{-0.09} M_{\odot}$ (at 90% CI) [61], and GW200210, with a secondary mass of $M_2 = 2.83^{+0.47}_{-0.42} M_{\odot}$ [62]. Conversely, GW230529 features a heavier primary component with a mass of $M_1 = 3.6^{+0.8}_{-1.2} M_{\odot}$ (at 90% CI) [63], placing it at the boundary between neutron stars and black holes. The secondary component of GW190814 has previously been interpreted as the remnant of an earlier merger that subsequently acquired a more massive black hole companion through dynamical exchange encounters in a globular cluster [61].

In addition to these massive objects, some new results for lower mass CSs, which are awaiting confirmation, have been reported. The X-ray spectrum of the central compact object within the supernova remnant HESS J1731-347 was modeled and in combination with the distance estimates from Gaia observations yielded a very low mass $M = 0.77^{+0.20}_{-0.17} M_{\odot}$ and a relatively small radius $R = 10.4^{+0.86}_{-0.78}$ km (at 68.3% CI) [64]. According to this estimation, the star can be either the lightest neutron star with conventional models of dense matter or a strange star [65–70]. The analysis of Ref. [64], however, has been questioned, in particular, their use of the object’s distance and uniform-temperature carbon atmosphere model, see Ref. [71]. It has been also argued that such a model does not perform well on longer-exposure XMM-Newton data from 2014 for the same source. Instead, a model featuring two hot regions emitting blackbody radiation from the surface of a star of mass $\sim 1.4 M_{\odot}$, provides a better description of this spectrum [71]. Very recently, the pulse profile modeling for the accretion-powered millisecond pulsar XTE J1814-338 with its thermonuclear burst oscillations, provided puzzling values for the mass and radius, $M = 1.21^{+0.05}_{-0.05} M_{\odot}$ and $R = 7.2^{+0.3}_{-0.4}$ km (at 68.3% CI) [72].

B. Summary of nucleonic models of dense matter

The EoS for dense matter in CSs can be constructed using various approaches, including *ab initio* calculations [73–76], density functional methods [77–80], and meta-type models [16, 81, 82], which provide a more schematic representation by parametrizing nuclear saturation properties. These models can also be linked to heavy-ion collision data [83, 84].

Ab initio calculations start with the nuclear force constrained by few-body bound states and scattering phase-shifts, but are computationally expensive, making it impractical to generate large ensembles of EoSs covering a broad nuclear parameter space. While chiral effective field theory (χ EFT) provides a systematic low-energy expansion, its applicability is currently limited to densities below $\rho < 2\rho_{\text{sat}}$. Consequently, extrapolations to higher densities often rely on physics-agnostic models [1, 10, 73, 85].

Meta-type models offer computational efficiency but primarily encode bulk nuclear matter properties, limiting their applicability to finite nuclei [16, 81, 82]. Density functionals, on the other hand, provide a balance between computational speed and versatility, allowing for EoS calculations while remaining applicable to finite nuclear systems [77–80]. This makes them particularly well-suited for integrating nuclear experimental data with astrophysical observations.

The covariant density functional (CDF) models provide a rigorous framework to address the full range of available data on nuclear systems, ranging from the atomic chart to the astrophysics of CSs, for reviews see Refs. [77, 79, 80, 86, 87]. These models were instrumental in addressing successfully such astrophysics problems as the hyperon puzzle in conjunction with two-solar mass CSs and the TD inference of the GW170817 event. The CDF models are separated into broad classes which (a) have non-linear meson contributions to the effective Lagrangian and (b) keep only linear coupling but impose density-dependence of the coupling, which captures the medium modifications of the meson-nucleon vertices. The mesons effectively considered, and their self- or cross-couplings in the former class or the explicit forms of density-dependences of the couplings in the latter class, are commonly flexible in order to address specific issues. Consequently, their predictions, are somewhat model-dependent, as different density functionals result in different dependences on density, see reviews [77, 79, 80].

II. DENSITY-DEPENDENT COVARIANT DENSITY FUNCTIONALS FOR NUCLEONIC MATTER

In this work, we use the standard form of CDF in which Dirac baryons are coupled to meson fields with density-dependent couplings [77, 80, 88–90]. The theory is Lorentz invariant and preserves causality when applied to high-density matter. The baryons interact via exchanges of σ , ω , and ρ mesons, which comprise the minimal set necessary for a quantitative description of nuclear phenomena.

We concentrate on cold, neutrino-free, catalyzed stellar matter. The Lagrangian with nucleonic degrees of freedom reads $\mathcal{L} = \mathcal{L}_N + \mathcal{L}_M + \mathcal{L}_I$, where the nucleonic Lagrangian is given by

$$\mathcal{L}_N = \sum_{N=n,p} \bar{\psi}_N \left[\gamma^\mu (i\partial_\mu - g_\omega \omega_\mu - g_\rho \boldsymbol{\tau} \cdot \boldsymbol{\rho}_\mu) - (m_N - g_\sigma \sigma) \right] \psi_N, \quad (1)$$

where ψ_N are the nucleonic Dirac fields with masses m_N , $\boldsymbol{\tau}$ is the vector of isospin Pauli matrices with τ_3 being its third

TABLE I. Nucleon and meson masses (in units of MeV) adopted in the CDF parametrization.

m_N	m_σ	m_ω	m_ρ
939.0000	550.1238	783.0000	763.0000

component, and σ , ω_μ , and ρ_μ represent the mesonic fields that mediate the interaction among nucleon fields with the corresponding coupling constants g_σ , g_ω and g_ρ , respectively. The remaining pieces of the Lagrangian correspond to the mesonic, and leptonic contributions, respectively [77, 80].

The particle masses adopted in the present analysis are listed in Table I, according to the widely used DD-ME parametrization [89, 90]. Note that the mass of the σ meson m_σ , which is supposed to represent the two- π -exchange contribution to the nuclear force is not known with precision and lies around 500 MeV. The properties of the infinite nuclear matter described by the present model depend only on the ratios of coupling constants and the corresponding meson masses [91, 92], and our results do not change with variation of σ meson mass m_σ , as its variations are equivalently encoded into the variations of g_σ as fixed m_σ .

The dependence of meson-nucleon couplings on the total baryon (vector) density is assumed to be

$$g_m(\rho) = g_m(\rho_{\text{sat}})f_m(r), \quad (2)$$

with a constant value at saturation density $g_m(\rho_{\text{sat}})$, and a function $f_m(r)$ that depends on the ratio $r = \rho/\rho_{\text{sat}}$. For the isoscalar sector, the density dependence is defined as

$$f_m(r) = a_m \frac{1 + b_m(r + d_m)^2}{1 + c_m(r + d_m)^2}, \quad m = \sigma, \omega. \quad (3)$$

Typically, parameters in Eq. (3) are not independent because the following five conditions are imposed [89, 90]:

$$f_m(1) = 1, \quad f'_m(0) = 0, \quad f''_\sigma(1) = f''_\omega(1), \quad (4)$$

which reduce the number of free parameters to three, i.e., a_σ , d_σ and d_ω . The rational function (3) has an advantage in contrast to polynomial or exponential forms, because it mimics the vertex functionals in Dirac-Brueckner computations that were extracted by mapping the self-energies in the local density approximation [88]. It is applicable over a wide density range covered by Dirac-Brueckner theory and converges to a constant at high densities. For the isovector sector, the density dependence is taken in an exponential form:

$$f_\rho(r) = \exp[-a_\rho(r - 1)]. \quad (5)$$

From Euler-Lagrangian equations, one can deduce the equations of motion for the constituent fields. In the Hartree mean-field approximation, the meson fields are replaced with their respective expectation values, $\bar{\sigma} = \langle \sigma \rangle$, $\bar{\omega} = \langle \omega_0 \rangle$ and $\bar{\rho} = \langle \rho_{0,3} \rangle$, which are in fact functions of vector or scalar density [80, 93]. The energy density and pressure of stellar matter

can be expressed, respectively, as

$$\begin{aligned} \varepsilon = & \frac{1}{2}m_\sigma^2\bar{\sigma}^2 + \frac{1}{2}m_\omega^2\bar{\omega}^2 + \frac{1}{2}m_\rho^2\bar{\rho}^2 \\ & + \frac{1}{2\pi^2} \sum_{N=n,p} (2J+1) \int_0^\infty dk k^2 E_N^k f(E_N^k) \\ & + \frac{1}{\pi^2} \sum_{l=e,\mu} \int_0^\infty dk k^2 E_l^k f(E_l^k), \end{aligned} \quad (6a)$$

$$\begin{aligned} P = & -\frac{1}{2}m_\sigma^2\bar{\sigma}^2 + \frac{1}{2}m_\omega^2\bar{\omega}^2 + \frac{1}{2}m_\rho^2\bar{\rho}^2 + \rho_N \Sigma_R \\ & + \frac{1}{6\pi^2} \sum_{N=n,p} (2J+1) \int_0^\infty dk \frac{k^4}{E_N^k} f(E_N^k) \\ & + \frac{1}{3\pi^2} \sum_{l=e,\mu} \int_0^\infty dk \frac{k^4}{E_l^k} f(E_l^k), \end{aligned} \quad (6b)$$

where $2J+1$ is the baryon degeneracy factor, f is the Fermi distribution functions, $E_N^k = \sqrt{k^2 + M_D^{*2}}$ and $E_l^k = \sqrt{k^2 + m_l^2}$ are the single-particle energies of nucleons and leptons respectively. The lepton mass m_l can be taken equal to its free-space value. The effective Dirac mass is defined as

$$M_D^* = m_N - g_\sigma \bar{\sigma}, \quad (7)$$

which is important for a quantitative description of finite nuclei, e.g., spin-orbit splitting [94]. The rearrangement term Σ_R in Eqs. (6) arises from the density dependence of meson-baryon couplings and is included to ensure thermodynamical consistency. It is seen that at zero temperature, the energy density and pressure of stellar matter are functions of baryonic density only.

It is now clear that if we fix in the Lagrangian (1) the nucleon and meson masses to be (or be close to) the ones in the vacuum then properties of infinite nuclear matter can be computed uniquely in terms of seven adjustable parameters. These are the three coupling constants at saturation density (g_σ , g_ω , g_ρ), and four parameters (a_σ , d_σ , d_ω , a_ρ) that control their density dependence. We further require conditions of weak equilibrium and charge neutrality that prevail in CSs. Combined with the field equations for baryons and mesons, they allow one to determine the equilibrium composition ρ_N and ρ_l at a given baryon number density and, thus, determine the EoS of stellar matter.

The energy density of isospin asymmetric matter is customarily split into an isoscalar term and an isovector term:

$$\varepsilon(\rho, \delta) \simeq E_0(\rho) + E_{\text{sym}}(\rho) \delta^2 + \mathcal{O}(\delta^4) \quad (8)$$

where $\rho = \rho_n + \rho_p$ is the baryonic density, with $\rho_{n(p)}$ denoting the neutron (proton) density, $\delta = (\rho_n - \rho_p)/\rho$ is the isospin asymmetry, and $E_0(\rho)$ and $E_{\text{sym}}(\rho)$ are, respectively, the energy of symmetric matter and the symmetry energy, which at densities close to the saturation ρ_{sat} can be further Taylor expanded as

$$E_0(\rho) \approx E_{\text{sat}} + \frac{1}{2!} K_{\text{sat}} \chi^2 + \frac{1}{3!} Q_{\text{sat}} \chi^3 + \frac{1}{4!} Z_{\text{sat}} \chi^4, \quad (9a)$$

$$E_{\text{sym}}(\rho) \approx J_{\text{sym}} + L_{\text{sym}} \chi + \frac{1}{2!} K_{\text{sym}} \chi^2 + \frac{1}{3!} Q_{\text{sym}} \chi^3, \quad (9b)$$

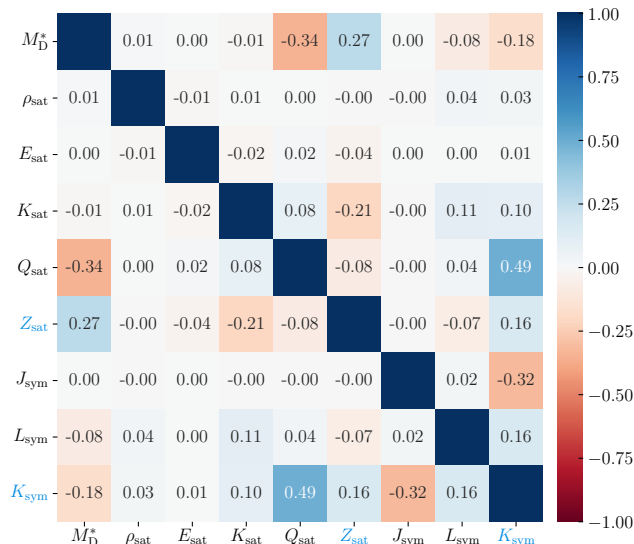


FIG. 2. Pearson correlation matrix for variation of nuclear characteristic parameters at saturation density, after applying (only) the SNM constraints at saturation density. Note that the higher-order parameters Z_{sat} and K_{sym} marked in blue color are predictions of the CDF model once the lower-order parameters are fixed.

where $\chi = (\rho - \rho_{\text{sat}})/3\rho_{\text{sat}}$. The coefficients of the expansion are known as *nuclear matter characteristics at saturation density*, namely, *binding energy* E_{sat} , *incompressibility* K_{sat} , the *skewness* Q_{sat} in the isoscalar sector, and the *symmetry energy* J_{sym} and its *slope parameter* L_{sym} in the isovector sector. Given the five macroscopic characteristics together with the preassigned values of ρ_{sat} and M_D^* , one can determine uniquely the seven adjustable parameters of the density functional defined above.

In Eqs. (9), we truncate the expansion at different orders in density in the isoscalar and isovector sectors, while also presenting higher-order coefficients for each sector—specifically, Z_{sat} , K_{sym} and Q_{sym} . These coefficients are, in fact, predictions derived from the lower-order parameters, because the

TABLE II. Symmetric nuclear matter (SNM) characteristics at saturation density and pure neutron matter (PNM) properties from χ EFT. These parameters are used to constrain the CDF parameters. The prior distributions assumed for the quantities are either a Gaussian distribution (G) or a uniform distribution (U).

	No.	Quantity	Unit	Interval	Prior
SNM	1	M_D^*	m_N	0.60 ± 0.05	G
	2	ρ_{sat}	fm^{-3}	0.153 ± 0.005	G
	3	E_{sat}	MeV	-16.1 ± 0.2	G
	4	K_{sat}	MeV	230 ± 40	G
	5	Q_{sat}	MeV	$[-1000, 1500]$	U
	6	J_{sym}	MeV	32.5 ± 2.0	G
	7	L_{sym}	MeV	$[0, 100]$	U
PNM	8	$P(\rho)$	MeV fm^{-3}	N^3LO	G
	9	$\epsilon(\rho)$	MeV fm^{-3}	N^3LO	G

latter uniquely fix the parameters of our CDF. The correlation matrix among these coefficients, shown in Fig. 2, is obtained from the posterior distribution using only the symmetric nuclear matter (SNM) constraints at saturation density, as listed in the upper panel of Table II. The results indicate that most of these coefficients exhibit little to no correlation, except for the pair (M_D^*, Q_{sat}) , which still shows a relatively weak correlation of approximately 0.3 (Pearson coefficient). Importantly, this framework allows for the independent variation of specific macroscopic characteristics within their acceptable ranges while keeping others fixed. This enables a systematic investigation of how these variations influence the EoS of dense matter and the properties of CSs [95, 96].

III. BAYESIAN INFERENCE FRAMEWORK

Bayesian analysis allows us to infer the probability distribution of unknown parameters in a model by exploiting the information in observed data. This is accomplished via Bayes's theorem,

$$P(\theta|\mathbf{D}) = \frac{\mathcal{L}(\mathbf{D}|\theta)P(\theta)}{\int \mathcal{L}(\mathbf{D}|\theta)P(\theta)d\theta}, \quad (10)$$

where available knowledge on model parameters θ is expressed as a prior distribution $P(\theta)$, by combining with observational data \mathbf{D} in the form of a likelihood function $\mathcal{L}(\mathbf{D}|\theta)$, the posterior distribution $P(\theta|\mathbf{D})$ is updated with the information from measured variables. The denominator is a normalization factor and acts as the evidence of data.

The present CDF-type EoS is specified by seven adjustable parameters in our analysis,

$$\theta_{\text{EoS}} = (g_\sigma, g_\omega, g_\rho, a_\sigma, d_\sigma, d_\omega, a_\rho), \quad (11)$$

for which we take uniform prior distributions with the intervals listed in Table III. Equivalently, the mapping to nuclear matter characteristics $(M_D^*, \rho_{\text{sat}}, E_{\text{sat}}, K_{\text{sat}}, Q_{\text{sat}}, J_{\text{sym}}, L_{\text{sym}})$, allows us to express the gross properties of CSs in terms of physically transparent quantities.

In our process of sampling, for each sample of parameters in Eq. (11) we first calculate the remaining five non-free parameters $(b_\sigma, c_\sigma, a_\omega, b_\omega, c_\omega)$ in the isoscalar sector from

TABLE III. The minimal (“min”) and maximal (“max”) values of the variation range of the CDF parameters at saturation density over which uniform prior distributions have been assigned.

No.	Parameter	min	max
1	g_σ	7.5	12.5
2	g_ω	9.5	15.5
3	g_ρ	2.5	5.0
4	a_σ	1.0	2.0
5	d_σ	0.0	1.5
6	d_ω	0.0	1.5
7	a_ρ	0.0	1.5

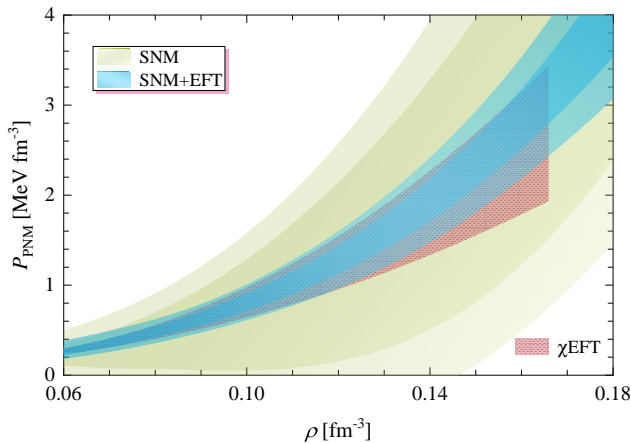


FIG. 3. Posterior distributions for the pressure of low-density neutron matter at 68.3% and 95.4% CIs, after applying either the SNM constraints at saturation density only (labeled SNM), or additionally the χ EFT constraints (labeled SNM+EFT).

Eq. (4) with a reference density ρ_{ref} . Given these twelve parameters and ρ_{ref} we can readily compute the seven nuclear matter characteristics at saturation density listed in Table II. The value of ρ_{ref} is updated each time, simultaneously with the five non-free parameters, in an iterative process, until the requirement $\rho_{\text{ref}} = \rho_{\text{sat}}$ is reached. At this stage, we have determined all the relevant parameters for the prior samples. We then compute the core EoS of stellar matter by incorporating the additional conditions of weak equilibrium and charge neutrality, which govern the composition of CSs. To ensure consistency, we smoothly match our core EoS to the crust EoS from Refs. [97, 98] at the crust-core transition density $0.5\rho_{\text{sat}}$. Finally, the global properties of CSs, including mass, radius, and TD, are obtained by integrating the Tolman-Oppenheimer-Volkoff equations [99, 100] and the associated equations for TD [101, 102].

In the present analysis, we employ the Python implementation of the Bayesian inference tool MULTINEST [103–105], which makes use of the Nested Sampling technique, to generate the posterior samples and estimate the marginalized distributions. The distributions presented for each run are counted from posterior samples of $\sim 3 \times 10^4$ EoSs to ensure the robustness of the inferred results. Below, we present a detailed discussion of the prior and likelihood we adopted in the current analysis.

A. Nuclear matter properties

The coefficients of the lower-order terms in the expansions (9), specifically E_{sat} , K_{sat} and J_{sym} , are well constrained. Additionally, the Dirac effective mass M_{D}^* at saturation density — crucial for an accurate description of finite nuclear phenomena, including spin-orbit splitting — is also well constrained. In contrast, the higher-order coefficients, such as Q_{sat} and L_{sym} remain less well determined, though they serve as asymptotic boundary conditions for the parametrization of

CDF models. For parameters known to within approximately 10%, we assume Gaussian prior distributions, while, for those with greater uncertainties, we adopt uniform priors. The mean values and standard deviations, or the respective parameter intervals, are summarized in Table II. Notably, we consider broader ranges for Q_{sat} and L_{sym} to encompass the possible values suggested by various works [81, 90, 106–110].

The Gaussian likelihood function for parameter i is defined as

$$\mathcal{L}_{\text{NM},i}(\theta_{\text{EoS}}) = \frac{1}{\sqrt{2\pi}\sigma_i} \exp\left[-\frac{1}{2}\left(\frac{d_i - \mu_i(\theta_{\text{EoS}})}{\sigma_i}\right)^2\right], \quad (12)$$

where d_i and σ_i are the datum and its standard uncertainty, respectively, and μ_i the corresponding model value. For quantities Q_{sat} and L_{sym} , the likelihood functions are implemented as Heaviside step functions of the form

$$\mathcal{L}_{\text{NM},i}(\theta_{\text{EoS}}) = H_{\pm}[d_i^{\text{cut}} - \mu_i(\theta_{\text{EoS}})], \quad (13)$$

where the model value μ_i is constrained from above or below by the sharp cutoff values d_i^{cut} .

In addition to the constraints above, we incorporate results for pure neutron matter based on chiral effective field theory (χ EFT) interactions which constrain the low-density regime of nucleonic EoS. In practice, we utilize the N³LO calculations from Ref. [73] to extract the energy per particle and pressure at densities of 0.08, 0.12, and 0.16 fm⁻³, which serve as constraints in our analysis. We further assume that the associated uncertainties follow a Gaussian distribution at the 68.3% CI. This approach allows us to retain models that fall outside the strict χ EFT band, rather than discarding them outright. It is worth noting that the uncertainty band reported in Ref. [73] lies within the broader range of results obtained from various χ EFT interactions compiled in Ref. [83].

To illustrate the influence of nuclear matter constraints, Fig. 3 presents the pressure distributions for low-density neutron matter at 68.3% and 95.4% CIs. These distributions are shown for cases where only the symmetric nuclear matter (SNM) constraints at saturation density are applied, as well as when the additional χ EFT constraint is included. The corresponding mass-radius (M - R) distributions derived from each posterior are displayed in Fig. 4. It is evident that our CDF model can generate a broad range of EoSs, encompassing the majority of current mass and radius inferences, as summarized in Fig. 1.

Those CDF parametrizations that are compatible with the χ EFT are soft at low densities and remain so up to $2\text{--}3\rho_{\text{sat}}$. More quantitatively, they have the value of symmetry energy and its slope at nuclear saturation density within the range $29.5 \leq J_{\text{sym}} \leq 33.5$ MeV and $35 \leq L_{\text{sym}} \leq 65$ MeV (at 95.4% CI), respectively. This leads to small radii for canonical-mass $1.4 M_{\odot}$ stars, $R_{1.4} \lesssim 13.5$ km, as shown in Fig. 4. More details on the posteriors of nuclear matter parameters are discussed in Subsec. IV B.

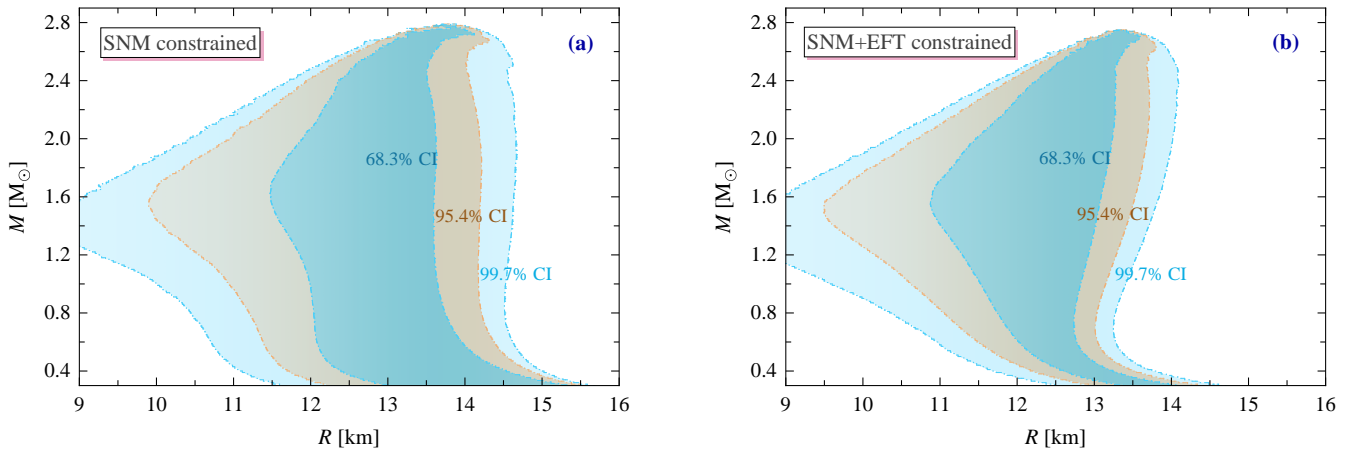


FIG. 4. Posteriors for mass-radius distributions at 68.3%, 95.4% and 99.7% CIs, after applying either the SNM constraints at saturation density only (left panel), or additionally the χ EFT constraints (right panel).

B. Astrophysical observations

We next describe our implementations of the likelihoods for various CS measurements, and assume that the datasets of different observed stars are independent.

1. NICER data

To date, the NICER collaborations have delivered the joint measurement of mass and radius through pulse profile modeling of four millisecond pulsars: a massive $\sim 2.1 M_\odot$ star PSR J0740+6620 and two canonical-mass $\sim 1.4 M_\odot$ stars PSR J0030+0451 and PSR J0437-4715, and a low-mass $\sim 1 M_\odot$ one PSR J1231-1411. We construct our likelihood functions for each of the sources using the Gaussian kernel density estimation (KDE) with the released posterior (M, R) samples \mathcal{S}_i ,

$$\mathcal{L}_{\text{NICER}, i}(\theta_{\text{EoS}}) = \text{KDE}(M, R | \mathcal{S}_i), \quad (14)$$

where the mass M and radius R for the star are functions of its central pressure and of the sampled EoS parameters. For the present analysis, we implement the following measured (M, R) samples as shown in Fig. 1 and listed below. The final likelihood is the product of four likelihoods for each of these sources.

- PSR J0740+6620 (hereafter J0740). For this heavy binary pulsar, we incorporate estimates from Refs. [39, 41, 42]. The representative estimates used in this study were obtained from a joint NICER and XMM-Newton analysis of the 2018-2022 dataset, based on the preferred ST-U model, which provides a more comprehensive treatment of the background [39].
- PSR J0437-4715 (J0437). We use the first mass and radius estimates for this brightest pulsar by using the 2017-2021 NICER X-ray spectral-timing data from Ref. [43]. The preferred CST+PDT model used informative priors on mass, distance, and inclination from

PPTA radio pulsar timing data, taking into account constraints on the non-source background and validating against XMM-Newton data [43].

- PSR J0030+0451 (J0030). For this isolated pulsar, we use two alternative mass and radius estimates from the reanalysis of 2017-2018 data, as reported in Ref. [40]. The two estimates are based on the joint analysis of NICER and XMM-Newton data which are labeled as ST+PDT and PDT-U. The ST+PDT results are more consistent with the magnetic field geometry inferred for the gamma-ray emission for this source [40, 111]. The PDT-U is the most complex model tested in Ref. [40] and is preferred by the Bayesian analysis.
- PSR J1231-1411 (J1231). The inference results obtained with the preferred PDT-U model show a strong sensitivity to the choice of radius priors, with stable and likely converged outcomes achieved only under constrained radius priors. We consider the mass and radius estimates from the preferred PDT-U model with limited radius priors given in Ref. [44]. One estimate limited the radius to be consistent with the previous observational constraints and EoS analyses (model (i)), and the other estimate used an uninformative prior for which the radius was limited to range 10-14 km (model (ii)).

For the sake of completeness, we briefly describe the pulse profile modelings mentioned above. In model ST-U each of the two hot spots is described by a single spherical cap; in CST+PDT there is a single temperature spherical spot with two components, one emitting and one masking; in ST+PDT the primary (ST) is described by a single spherical cap and the secondary (PDT) by two components, both emitting; in PDT-U each of the two hot spots is described by two emitting spherical caps. For details see Refs. [39, 40, 43, 44].

TABLE IV. Astrophysical constraints used for the scenarios in the present work.

Scenario	J0348	J0952	GW (2)	J0740 ST-U	J0437 CST+PDT	J0030		J1231		HESS J1731
						ST+PDT	PDT-U	PDT-U (i)	PDT-U (ii)	
B1	×		×	×	×	×		×		
B2	×		×	×	×	×		×		×
B3	×	×	×	×	×	×		×		
B4	×	×	×	×	×	×		×		×
F1	×		×	×	×		×		×	
F2	×		×	×	×		×		×	×
F3	×	×	×	×	×		×		×	
F4	×	×	×	×	×		×		×	×

2. GW data

The GW170817 [33] and GW190425 [36] events are the only two confirmed (and most likely) binary neutron star mergers detected during past observing runs of the LIGO-Virgo-Kagra collaboration. When incorporating measurements from a single GW event, the likelihood function used for Bayesian inference can be expressed as

$$\mathcal{L}(\boldsymbol{\theta}_{\text{GW}}) \propto \exp\left(-2 \int \frac{|d(f) + h(\boldsymbol{\theta}_{\text{GW}}, f)|^2}{S(f)} df\right), \quad (15)$$

where $S(f)$, $d(f)$, and $h(\boldsymbol{\theta}_{\text{GW}}, f)$, respectively, represent the power spectral density of the detector noise, the detected strain signal, and the expected strain from a waveform model. The vector $\boldsymbol{\theta}_{\text{GW}}$ includes parameters that are particularly useful to infer EoS properties, $\boldsymbol{\theta}_{\text{GW}}^{\text{EoS}}$, and nuisance parameters, $\boldsymbol{\theta}_{\text{GW}}^{\text{nuis}}$, that are essential when performing analysis on GW-emitting binaries. Including a dozen nuisance parameters, however, significantly slows down the sampling process and hence we calculate the likelihood through the high-precision interpolation in TOAST [112] that marginalizes over these parameters,

$$\mathcal{L}_{\text{GW},i}(\boldsymbol{\theta}_{\text{EoS}}) = F_i(\mathcal{M}, q, \Lambda_1, \Lambda_2), \quad (16)$$

where $\mathcal{M} = (M_1 M_2)^{3/5} / (M_1 + M_2)^{1/5}$ is the chirp mass, $q = M_1 / M_2$ is the mass ratio of the event i , and $\Lambda_1(M_1)$ and $\Lambda_2(M_2)$ the TDs of the individual stars. The TD is related to the component star's mass and radius through the underlying EoS and its radial profile.

3. Massive millisecond pulsars

To model the mass measurements of massive pulsars (MP), such as PSR J0348+0432 (hereafter J0948, [48]) and PSR J0952-0607 (J0952, [59]), we employ Gaussian distributions. The likelihood is then constructed using the cumulative density function of the Gaussian distribution

$$\mathcal{L}_{\text{MP},i}(\boldsymbol{\theta}_{\text{EoS}}) = \frac{1}{2} \left[1 + \text{erf}\left(\frac{M_{\text{max}}(\boldsymbol{\theta}_{\text{EoS}}) - M_i}{\sqrt{2}\sigma_i}\right) \right], \quad (17)$$

where $\text{erf}(x)$ is the error function, M_i and σ_i are the mean and the standard deviation of the mass measurement for the source i , respectively. We do not take into account the mass measurement for PSR J0740 [49, 50], to avoid a double counting with its NICER estimates.

4. HESS J1731-347

In the case of unusually light neutron star HESS J1731-347 (hereafter J1731), a consensus on its gross parameters has not been reached yet on the basis of observational modeling. Nevertheless, we tentatively incorporate this source into our analysis for theoretical exploration. Specifically, we adopt one of the two most reliable results from Ref. [64], which utilized the most advanced physical modeling and the most precise distance measurements available. Similar to the NICER sources, we apply the KDE method to the released model samples to generate the posterior distributions, which are then treated as the likelihood $\mathcal{L}_{\text{HESS}}(\boldsymbol{\theta}_{\text{EoS}})$.

IV. MULTIMESSENGER INFERENCES ON COMPACT STARS AND DENSE MATTER

We apply the theoretical and astrophysical constraints both selectively and in concert to elucidate the importance of the individual impacts of the ultra-compact low-mass star (HESS J1731) and the very high mass star (PSR J0952) as well as the overall picture that emerges from a combination of such constraints.

Before embarking onto detailed discussion we present the scenarios that we consider in Table IV. Specifically, we will examine two baseline scenarios, labeled B1 and F1, which share the same data for PSR J0437 and PSR J0740 but incorporate two different analyses for PSR J0030 using different models of the surface temperature patterns, and two different analyses for PSR J1231 using different radius priors. For each baseline scenario, we implement further the data for the ultra-compact low-mass star HESS J1731 (denoted as scenarios B2 and F2), and for the high-mass star PSR J0952 (denoted as scenarios B3 and F3). Finally we take into account both constraints (denoted as scenarios B4 and F4) in our analysis.

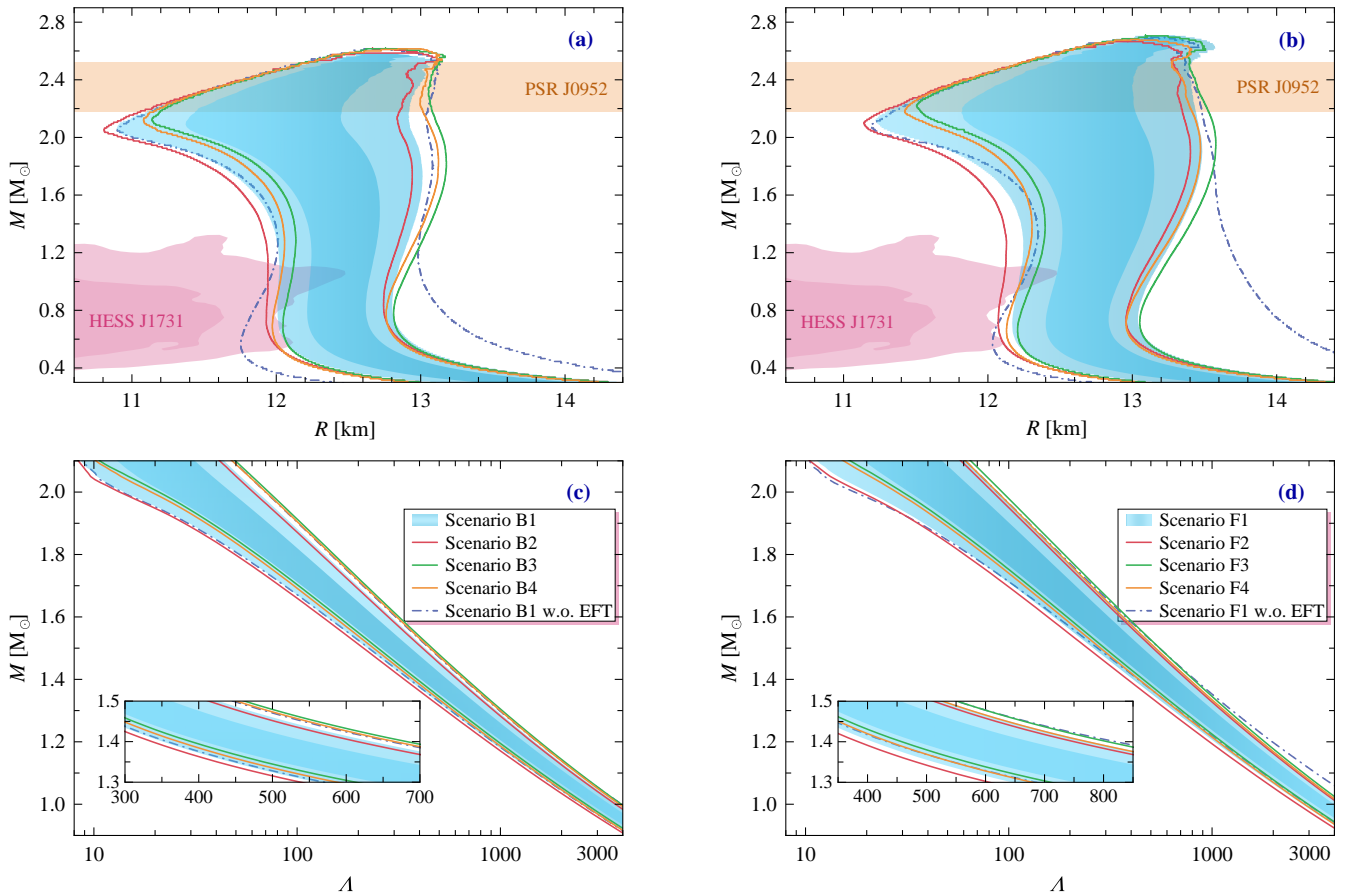


FIG. 5. Posteriors for mass-radius (upper panels) and mass-tidal deformability (lower panels) distributions under different astrophysical scenarios explored in this work. The shaded regions represent the distributions at 68.3% and 95.4% CIs for scenarios B (left panels) and F (right panels). The various color solid lines show the results at 95.4% CI for scenarios which take additionally into account the mass-radius estimates of HESS J1731 (B2 and F2), the mass measurement of PSR J0952 (B3 and F3), or both of these measurements (B4 and F4). Finally, the dash-dotted lines correspond to the scenarios which do not include the χ EFT constraints. In the lower panels, the insets magnify the TDs for typical masses of CSs involved in GW events. In the upper panels, the elliptical contours of the input mass-radius estimates of HESS J1731 and the band for the mass of PSR J0952 are shown as well for reference.

A. Implications for properties of compact stars

The new NICER estimates for PSR J0437 and J1231, combined with the reanalysis of PSR J0030, have enabled the construction of various scenarios incorporating different models of surface temperature distributions for pulsars. The scenarios B1 and F1 in Table IV represent two distinct combinations of the current NICER estimates for pulsars, corresponding to the softest and stiffest models, respectively; see also Ref. [31]. In scenario B1, the more compact estimates for PSR J1231 (PDT-U (i) model) and J0030 (ST+PDT model), favoring softer EoS at densities below 2 and $3\rho_{\text{sat}}$, respectively, are used and give rise to the tightest credible regions. In contrast, the widest credible regions are predicted in scenario F1, which incorporates less compact estimates for PSR J1231 (PDT-U (ii) model) and J0030 (PDT-U model).

Figure 5 shows the posteriors for M - R and M - Λ distributions within the scenarios B1 and F1, and Fig. 6 displays the corresponding probability distributions for the values of maximum mass M_{max} . For reference, we list here the selected

gross properties of CSs predicted from the baseline scenarios B1 and F1. The radius for a canonical-mass $1.4 M_{\odot}$ star is $R_{1.4} = 12.47^{+0.48}_{-0.50}$ (at 95.4% CI) for scenario B1 and $12.79^{+0.55}_{-0.56}$ for scenario F1. The corresponding TD is $\Lambda_{1.4} = 472^{+163}_{-121}$ for scenario B1 and 571^{+207}_{-162} (at 95.4% CI) for scenario F1. The maximum mass is $M_{\text{max}} = 2.20^{+0.23}_{-0.17} M_{\odot}$ and $2.32^{+0.24}_{-0.24} M_{\odot}$ respectively for scenarios B1 and F1. The latter scenario allows for a static CS interpretation for the secondary component of the GW190814 event [36], with a mass 2.50 - $2.67 M_{\odot}$ at 90% CI, and for the primary component of the GW230529 event [63], with a mass $3.6^{+0.8}_{-1.2} M_{\odot}$.

With additional constraints incorporated, the M - R distribution retains a similar overall structure. Notably, the 95.4% CI regions reveal remarkably narrow radius intervals for sub-canonical mass CSs ($M < 1.4 M_{\odot}$), typically around 1 km. In contrast, the widest radius variations are observed around $M \approx 2.0 M_{\odot}$.

Incorporating the mass and radius estimates for HESS J1731 results in only a slight shift—approximately 0.1 km—to the lower-radius side in the posterior region for sce-

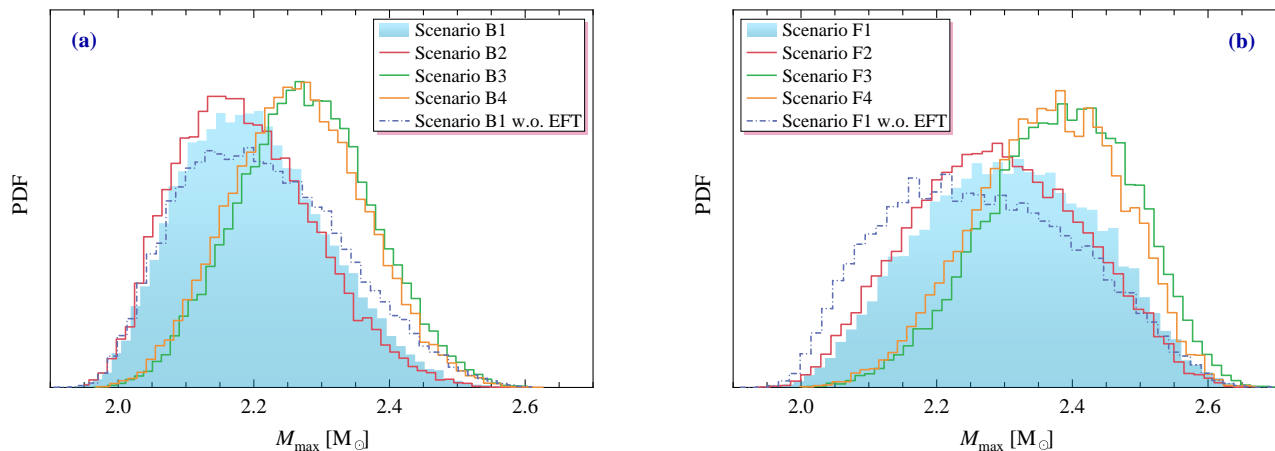


FIG. 6. Probability distribution functions (PDFs) for maximum mass M_{\max} under different astrophysical scenarios. The shaded regions represent the distributions for scenarios B1 (left panel) and F1 (right panel), while the various color solid lines correspond to the scenarios which take additionally into account the mass-radius estimates of HESS J1731 (B2 and F2), mass measurement of PSR J0952 (B3 and F3), or both of these two measurements (B4 and F4). The dash-dotted lines correspond to neglecting the χ EFT constraints in scenarios B1 and F1.

nario B2 (F2) compared to B1 (F1); see Fig. 5. As expected, the posterior distributions for tidal deformability (Λ) exhibit similar trends to the M - R posteriors due to the strong positive correlation between Λ and R for a given mass (e.g., Ref [47] and references therein). Consequently, the posterior region overlaps with the mass and radius estimates for HESS J1731 only at the 95.4% CI. Meanwhile, the impact on the maximum mass (M_{\max}) distribution remains negligible in scenarios B1 and B2 (F1 and F2); see Fig. 6. This suggests that the mass and radius measurements of four pulsars from NICER, combined with the TDs inferred from GW170817, GW190425 and the constraints from χ EFT calculations, primarily define the posterior region of the M - R distribution. The effect of the χ EFT constraint on the M - R posterior is particularly evident in scenarios B1 and F1 (Fig. 5), where it imposes a lower bound on the radii of sub-canonical-mass stars. Additionally, the mass and radius inferences derived for HESS J1731 shows only weak overlap with the M - R ellipse for PSR J1231 (Fig. 1), which limits the influence of HESS J1731 data in distinguishing viable EoSs.

Including the mass measurement for PSR J0952 instead, namely for scenario B3 (F3), the posterior region is shifted to a larger radius region by 0.1-0.4 km compared to scenario B1 (F1). A more significant difference appears for stars with mass $M > 1.4 M_{\odot}$. This is because the radii for sub-canonical-mass stars are well-constrained, while the NICER inferences for PSR J0030 and J0740, allow for radii larger than 14 km, which then allow stiffer high-density EoSs. As anticipated, the maximum mass M_{\max} is enlarged by $0.1 M_{\odot}$, with, in particular, a higher probability density for scenario F3; see Fig. 6. The maximum mass now is $M_{\max} = 2.28^{+0.20}_{-0.19} M_{\odot}$ and $2.39^{+0.19}_{-0.23} M_{\odot}$ respectively for scenarios B3 and F3. Meanwhile, the distributions of maximum mass M_{\max} is somewhat narrowed compared to scenarios B1 and F1, respectively.

Finally, incorporating both HESS J1731 and PSR J0952 data, namely for scenarios B4 and F4, the boundaries for the posterior regions are located well within the ranges set by the

two cases discussed above. The distributions of maximum mass M_{\max} are rather close to those of scenarios B3 and F3, respectively. To conclude, the M - R estimates for HESS J1731 and mass measurement for PSR J0952 affect only the finer details of the posterior compared to the case where these constraints are not included.

Reference [113] pointed out that the sign of the difference of the radii of CSs of masses 1.4 and $2.0 M_{\odot}$, $\Delta R = R_{1.4} - R_{2.0}$ is an indicator that the EoS softens (if positive) or stiffens (if negative) at high densities. Figure 7 illustrates the posterior distributions for the correlation between $R_{1.4}$ and $R_{2.0}$, and the correlation between the maximum mass M_{\max} and the radius difference ΔR . It is seen that the correlations between these parameters are similar across all scenarios. For scenarios B (B refers to B1–B4), the preference is for ΔR being positive, i.e., $R_{1.4} > R_{2.0}$, but for scenarios F, negative ΔR is allowed even at 68.3% CI. More details of correlations among properties of CSs will be discussed below in Subsec. IV C. The predicted key quantities of CSs under different astrophysical scenarios are summarized in the Appendix.

It is worth noting that across all the scenarios discussed, our CDF-based EoS not only maintains reasonable nuclear saturation properties (to be elaborated in the next subsection) but also supports maximum masses exceeding $\approx 2.5 M_{\odot}$. This contrasts with earlier studies of this type, which employed simplified forms of the density-dependent meson-baryon coupling functions (3) [18, 24, 28], offering less flexibility than the approach adopted in the present work. In fact, calculations based on the same CDF framework used here [22, 32], or on versions of CDF with more tunable parameters (beyond simple exponentials) [22, 23, 29, 32], have been able to construct models with $M \geq 2.5 M_{\odot}$, even when fewer observational constraints were applied.

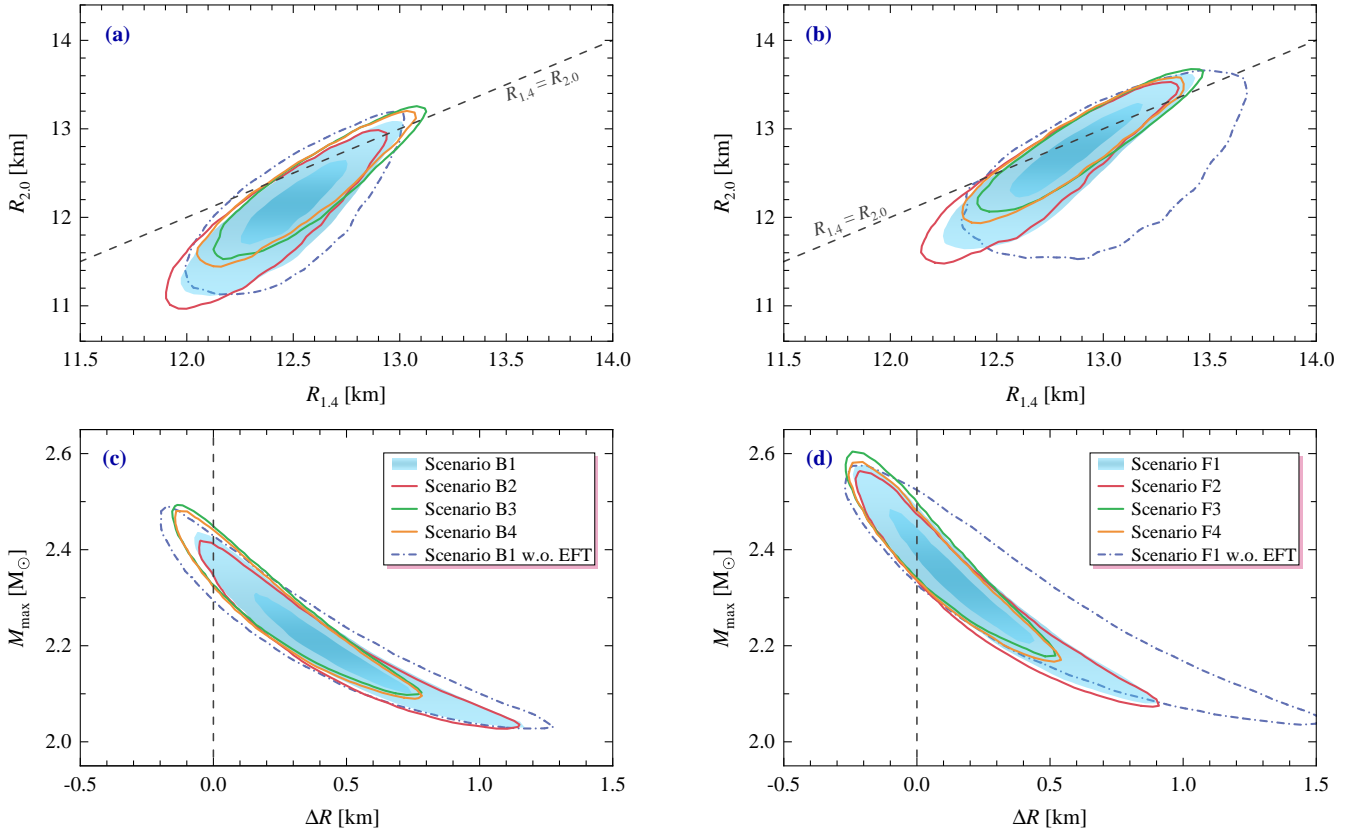


FIG. 7. Correlation between the radii $R_{2,0}$ and $R_{1,4}$ (upper panels), and the maximum mass M_{\max} and the radius-difference $\Delta R = R_{1,4} - R_{2,0}$ (lower panels) under different astrophysical scenarios. The shaded regions represent the distributions at 68.3% and 95.4% CIs for scenarios B1 (left panels) and F1 (right panels), while the various color solid lines correspond to 95.4% CI for the scenarios which take additionally into account the mass-radius estimates of HESS J1731 (B2 and F2), mass measurement of PSR J0952 (B3 and F3), or both of these two measurements (B4 and F4). The dash-dotted line for scenarios (B1 and F1) correspond to neglecting the χ EFT constraints.

B. Implications for properties of nucleonic EoS

In this subsection, we assess the properties of the nucleonic EoS. Figure 8 summarizes the posterior distributions for EoS used to generate the M - R posteriors in the previous subsection, as well as the corresponding proton fraction under different astrophysical scenarios. For scenarios B1 and B4 (F1 and F4), we show also the contours representing the positions of the respective $2.0 M_{\odot}$ and the maximum-mass M_{\max} configurations for reference. The differences for EoS posteriors among different scenarios are consistent with those for M - R posteriors.

For each scenario considered we find that the inclusion of HESS J1731 data produces slightly lower pressure for low-density regions compared to posteriors for baseline. This is in agreement with its low mass interval involved in modeling this object. The inclusion of PSR J0952 data produces noticeably higher pressure at high-densities, which is required to provide preference for values of $M_{\max} \sim 2.3$ - $2.4 M_{\odot}$. As expected, low-density $\rho \leq 2\rho_{\text{sat}}$ EoS posteriors are marginally affected by this additional constraint.

The impacts of the individual astrophysical constraints on EoS could be understood in terms of the nuclear mat-

ter characteristics at saturation density, which are shown in Fig. 9. For reference, we list here the selected characteristics predicted from the baseline scenarios B1 and F1. Scenario B1 features lower values for the incompressibility, $K_{\text{sat}} = 231.4^{+34.4}_{-33.3}$ MeV and negative values for the skewness, $Q_{\text{sat}} = -391.0^{+333.6}_{-170.2}$ MeV (at 68.3% CI) in the isoscalar sector, and symmetry energy $J_{\text{sym}} = 31.24^{+0.88}_{-0.86}$ MeV and its slope $L_{\text{sym}} = 46.73^{+5.94}_{-5.67}$ MeV in the isovector sector. The scenario F1 has higher values for $K_{\text{sat}} = 244.8^{+36.4}_{-34.7}$ MeV and allows for positive value for $Q_{\text{sat}} = -164.7^{+548.9}_{-280.1}$ MeV (at 68.3% CI) in the isoscalar sector, and $J_{\text{sym}} = 31.20^{+0.89}_{-0.88}$ MeV and $L_{\text{sym}} = 47.86^{+6.46}_{-6.27}$ MeV in the isovector sector. Note that in this scenario the value of Q_{sat} can further reach up to 900 MeV at a 95.4% CI. The correlations among nuclear characteristics at saturation density will be accessed below in Subsec. IV C.

Including additional constraints, it is seen that the lowest-order parameters E_{sat} and J_{sym} are almost identical among scenarios B (F). The parameter K_{sat} is reduced by 5-10 MeV ($< 5\%$) and L_{sym} is reduced by only 1-2 MeV ($< 5\%$) among scenarios B (F). These reductions are responsible for the softness required by HESS J1731 data in scenarios B2 or F2. In contrast, for scenarios B3 and F3 where the PSR J0952 data are included, such reductions mainly counter-

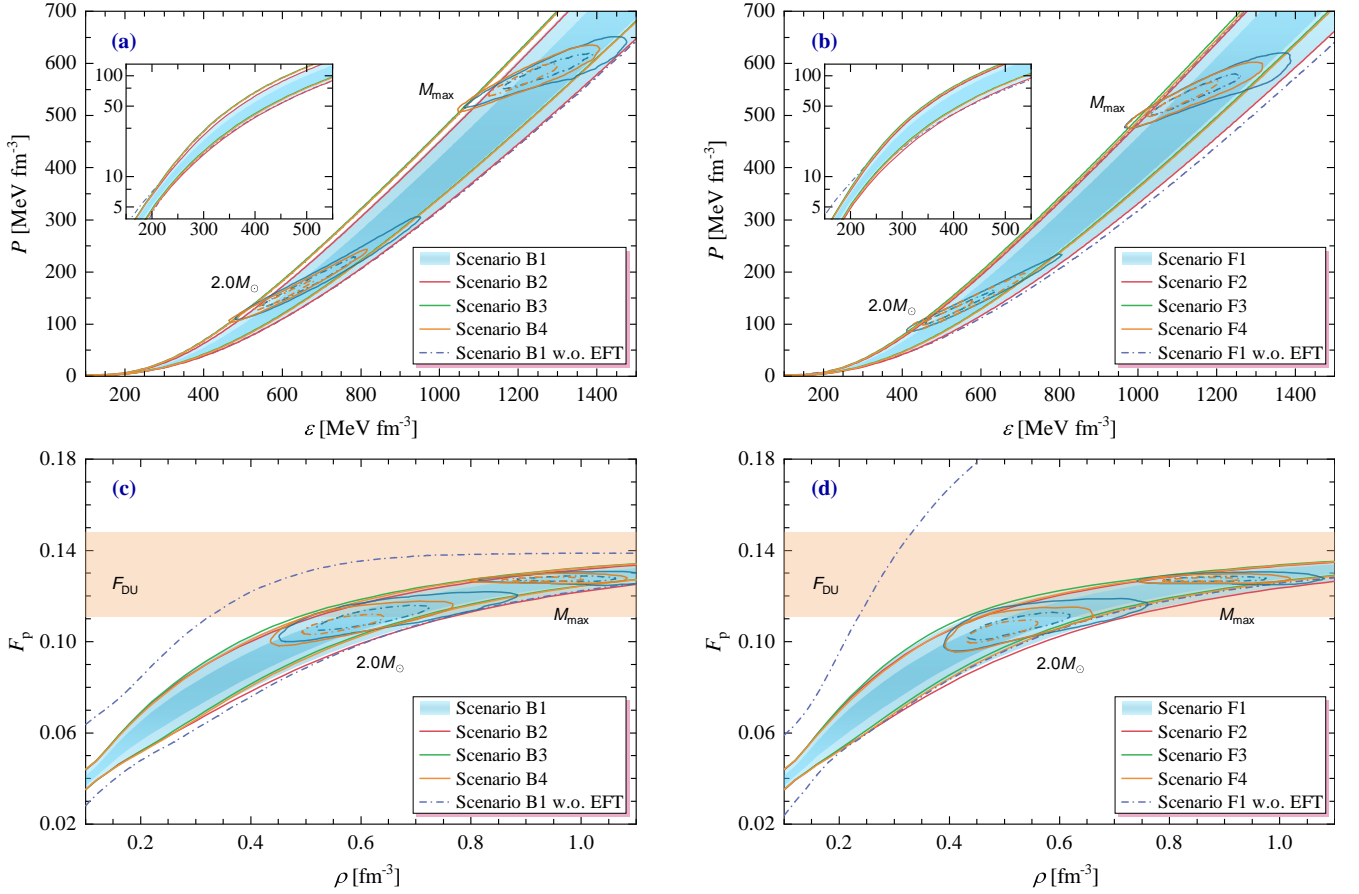


FIG. 8. Posteriors for the nucleonic compact-star EoS (upper panels) distribution and the proton fraction (lower panels) under different scenarios. The shaded regions represent the distributions at 68.3% and 95.4% CIs for scenarios B1 (left panels) and F1 (right panels), while the various color solid lines correspond to 95.4% CI for the scenarios which take additionally into account the mass-radius estimates of HESS J1731 (B2 and F2), the mass measurement of PSR J0952 (B3 and F3), and both of these two measurements (B4 and F4). The dash-dotted line for scenarios (B1 and F1) corresponds to neglecting the χ EFT constraint. In each panel, the contours show the corresponding distributions of the respective $2.0 M_{\odot}$ and the maximum-mass configurations for scenarios B1 (B4) and F1 (F4). In lower panels the orange bands labeled F_{DU} show the admissible threshold values for the onset of direct Urca (DU) cooling process.

vail the stiffness induced by the higher values of Q_{sat} and K_{sym} at low density regime, which now are increased up to $Q_{\text{sat}} = -215.0^{+435.7}_{-253.0}$ MeV and $K_{\text{sym}} = -96.8^{+24.0}_{-16.6}$ MeV (at 68.3% CI) for scenario B3, and to $Q_{\text{sat}} = 81.0^{+548.4}_{-386.6}$ MeV and $K_{\text{sym}} = -83.8^{+26.9}_{-19.5}$ MeV for scenario F3. Note that in our modeling, the parameters K_{sat} and Q_{sat} are quasi-independent of each other, which is in contrast to previous studies of this type CDF with simplified functions (3) for density dependence of isoscalar meson-nucleon couplings [18, 24, 28]. Since the isovector parameter K_{sym} is not entirely independent, its variations arise from slight adjustments in the two lower-order parameters, J_{sym} and L_{sym} .

In the lower panels of Fig. 8 the horizontal bands indicate the nucleonic direct Urca (DU) threshold. This band is, however, model dependent [114]. For μ^- free case the threshold value is 11.1%; in the limit of massless μ^- s, which is applicable for high densities matter, it yields an upper limit of 14.8%. As seen in this plot, due to the softness (dominated by χ EFT constraint) of the nucleonic EoS at low densities, the

DU process will be mostly disallowed in CSs with $M \leq 2 M_{\odot}$ if one utilizes the current CDF-based EoS. The same conclusion was reached in Refs. [14, 18, 32], where the density dependence of the ρ -meson coupling was also modeled using an exponential form. However, note that the DU threshold may be smoothed out due to short-range correlations which allow for finite width of the baryon spectral function in dense matter [115]. Moreover, non-nucleonic DU processes may still occur if hyperons or Δ -resonances appear in the inner cores of compact stars; see, for example, Refs. [93, 116, 117]. Alternatively, modifications to the density dependence of the ρ -meson coupling function can lead to an earlier onset of nucleonic DU processes, as discussed in Refs. [19, 23, 29, 32].

Finally, in Fig. 10 we show the posterior distributions for the pressure (upper panels) and symmetry energy (lower panels) of symmetric nuclear matter as a function of baryonic density under different astrophysical scenarios. In each panel we also include for reference the experimental constraints obtained from extensive, independent studies.

In the upper panels of Fig. 10, we show the constraints

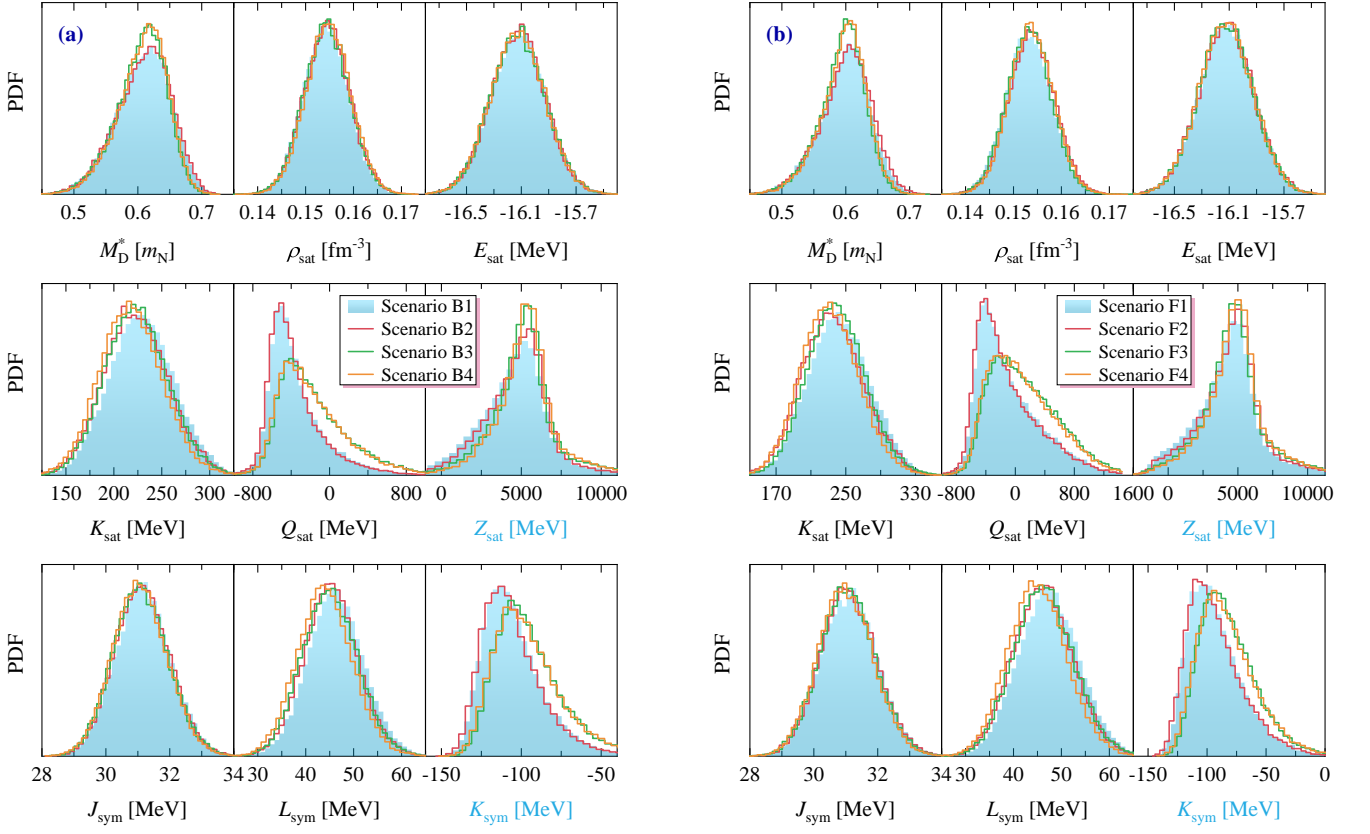


FIG. 9. Posterior distributions of nuclear matter saturation properties under different astrophysical scenarios. The shaded regions indicate the results for scenarios B1 (left panels) and F1 (right panels). The various color lines represent the results for scenarios that additionally incorporate the mass-radius estimates of HESS J1731 (B2 and F2), the mass measurement of PSR J0952 (B3 and F3), or both measurements combined (B4 and F4). Note that the higher-order characteristic parameters Z_{sat} and K_{sym} marked in blue color are predictions of those lower-order parameters in the present CDF.

for pressure obtained from heavy ion collision data. These include: (a) the constraint obtained by comparing measurements of collective flow from heavy-ion collisions with results from hadronic transport simulations using a set of EoSs (labeled cFlow) [118]; (b) the constraint obtained by reproducing in hadronic transport simulations with mean-field interactions the ratios of experimentally measured kaon yields in Au+Au and C+C collisions (Kanos) [119, 120], and (c) constraint obtained from the elliptic flow data measured by the FOPI collaboration together with simulations from isospin quantum molecular dynamics (QMD) (eFlow) [121]. It is seen that the 68.3% CI regions of the EoSs from scenarios from B1-B4 largely coincide with the HIC constraints, while the 95.4% CI regions of the EoSs from scenarios F1-F4 overlap with the constraints. Note, however, that these HIC constraints exhibit some model dependence, especially regarding the high-density behavior explored in collision simulations. Moreover, certain nuclear models used to interpret the experimental data do not support two-solar-mass CSs.

As is well known, determining the composition at high densities requires precise information on the density dependence of symmetry energy. As shown in the lower panels of Fig. 10, the predicted symmetry energy exhibits a remarkably narrow range. This is primarily due to the limited degrees of free-

dom in the isovector sector of the present CDF model, which includes only two parameters, both of which are strongly constrained by the χ EFT results for low-density pure neutron matter. Consequently, the behavior of symmetry energy near ρ_{sat} and at higher densities is predominantly governed by L_{sym} . This, in turn, explains the narrow band of proton fraction observed in the lower panels of Fig. 8.

For comparison, in the lower panels of Fig. 10 we also give the constraints on symmetry energy obtained from: (a) the comparison of the experimental measurements of isospin diffusion and the ratio of neutron and proton spectra in collisions of Sn+Sn to results from the improved QMD simulations (labeled HIC) [122]; (b) the studies of the ratio of the elliptic flow of neutrons and hydrogen nuclei in Au+Au collisions in the FOPI-LAND experiment (FOPI) [123]; (c) the use of neutron-to-charged fragments ratios measured in Au+Au collisions in the ASY-EOS experiment (ASY) [124]; and (d) nuclear structure studies involving excitation energies to isobaric analog states (IAS) [125]. Also shown in this plot is the 68.3% CI region consistent with the best fit of experimental data on the isospin diffusion in collision systems with a different proton-to-neutron ratios, neutron-to-proton energy spectra, and spectral pion ratios in Sn+Sn collisions (labeled FIT) [126]. It is clearly seen that our models are broadly con-

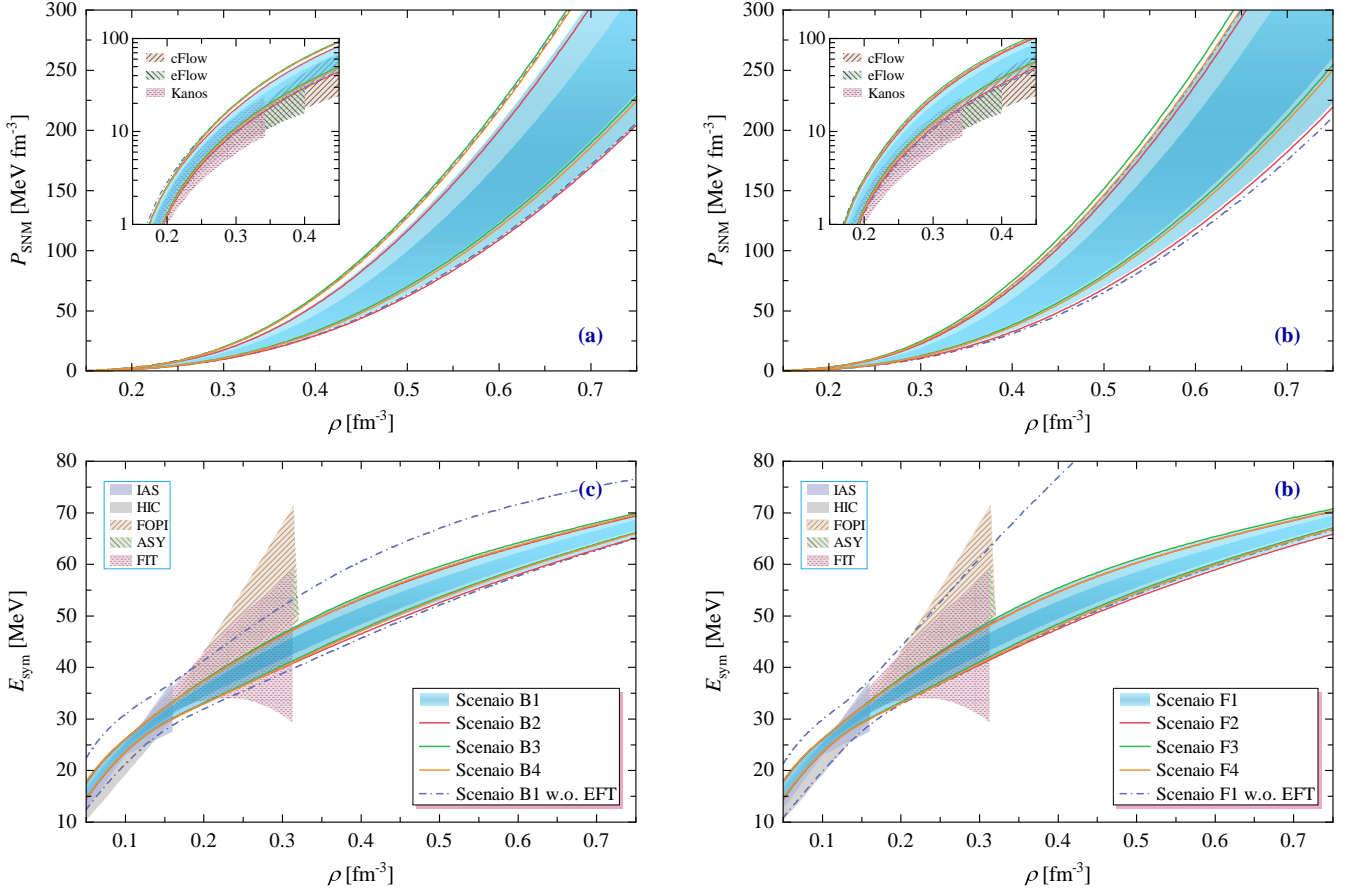


FIG. 10. Posterior distributions of pressure (upper panels) and symmetry energy (lower panels) as functions of baryonic density for symmetric nuclear matter under different astrophysical scenarios. The shaded regions indicate the 68.3% and 95.4% CIs for scenarios B1 (left panels) and F1 (right panels). Solid lines represent results at 95.4% CI incorporating additional constraints from the mass-radius estimates of HESS J1731 (B2 and F2), the mass measurement of PSR J0952 (B3 and F3), or both (B4 and F4). Dash-dotted lines correspond to scenarios where the χ EFT constraint is not applied. In the upper panels, the insets magnify the low-density regions. The constraints for pressure and symmetry energy obtained from hadronic transport simulations and/or nuclear structure studies are shown for comparison, see text for details.

sistent with these constraints. The predicted bulk quantities of nuclear matter at saturation density for different astrophysical scenarios are summarized in the Appendix.

C. Correlations of CDF parameters, nuclear characteristics, and compact-star properties

We now focus on the correlations of CDF parameters, nuclear matter characteristics and CS properties, and the correlations between two of them for representative scenarios. In Fig. 11, we show the posterior distributions on the CDF parameters for scenarios B1 and F1, respectively. For each, we include the seven adjustable parameters ($g_\sigma, g_\omega, g_\rho, a_\sigma, d_\sigma, d_\omega, a_\rho$) that describe the CDF and in addition the parameter a_ω . In these corner plots, we show the two-dimensional (2D) correlated probability distributions and along the diagonal one-dimensional (1D) probability distribution functions (PDFs). The elliptical nature of the 2D contour for a pair of parameters indicates the correlation existing between them, while a circular nature indicates no correlation.

In the 1D plots, we also display the results that applied only the constraints on the SNM characteristics at saturation density (labeled SNM) as well as those which combine these with the χ EFT computations (labeled SNM+EFT).

As anticipated the pair of parameters (g_σ, g_ω) displayed in Fig. 11 high correlation, as these are the parameters that determine the binding energy at saturation density. The pairs of (d_σ, d_ω) and (a_σ, a_ω) that control the density dependence of σ and ω mesons' couplings are also strongly correlated as they are constrained by the conditions (4). In addition, the two parameters (g_ρ, a_ρ) in the isovector sector were seen to be correlated already when only the χ EFT constraint is applied, and their PDFs are almost identically to those for scenarios B1 and F1, which means that the astrophysical constraints do not introduce any noticeable modifications.

In Fig. 12, we show nine nuclear characteristic parameters at saturation density, namely, ($M_D^*, \rho_{\text{sat}}, E_{\text{sat}}, K_{\text{sat}}, Q_{\text{sat}}$) in the isoscalar sector and ($J_{\text{sym}}, L_{\text{sym}}$) in the isovector sector, and for each sector we show an additional higher-order parameter (Z_{sat} and K_{sym} , respectively) which are predictions based on values of the lower-order parameters that fix the param-

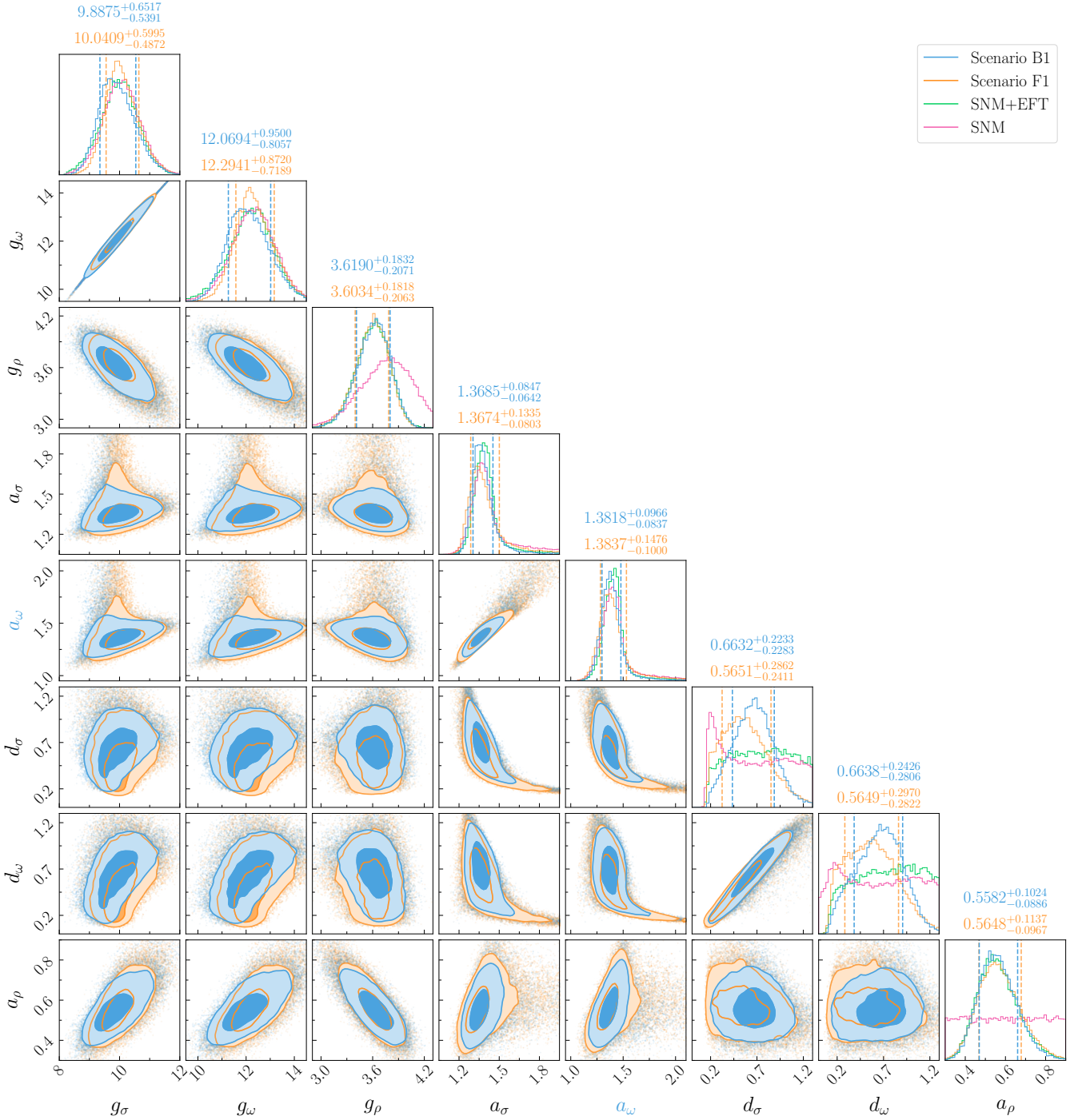


FIG. 11. Posterior distributions of eight CDF parameters under astrophysical scenarios B1 and F1. The light- and dark-shaded regions represent the 68.3% and 95.4% CIs for the two-dimensional distributions, while the one-dimensional posteriors for each parameter are shown along the edges, with vertical lines indicating the 68.3% CI. For comparison, results considering only the constraints from symmetric nuclear matter characteristic parameters (labeled SNM) and those including additional EFT computations (labeled SNM+EFT) are provided in the one-dimensional plots. The parameter a_ω (highlighted in blue) is not a free parameter in the present CDF framework.

ters of the present CDF. It is seen that the PDFs for parameters (M_D^* , ρ_{sat} , E_{sat} , K_{sat}) in the isoscalar sector and J_{sym} in the isovector sector behave similarly in different cases shown in Fig. 12 as the Gaussian distribution is applied to the priors.

When the χ EFT constraint is applied, the PDF for the slope parameter L_{sym} exhibits a Gaussian-like behavior. This arises from its strong correlation with J_{sym} , despite the assumption of a uniform prior.

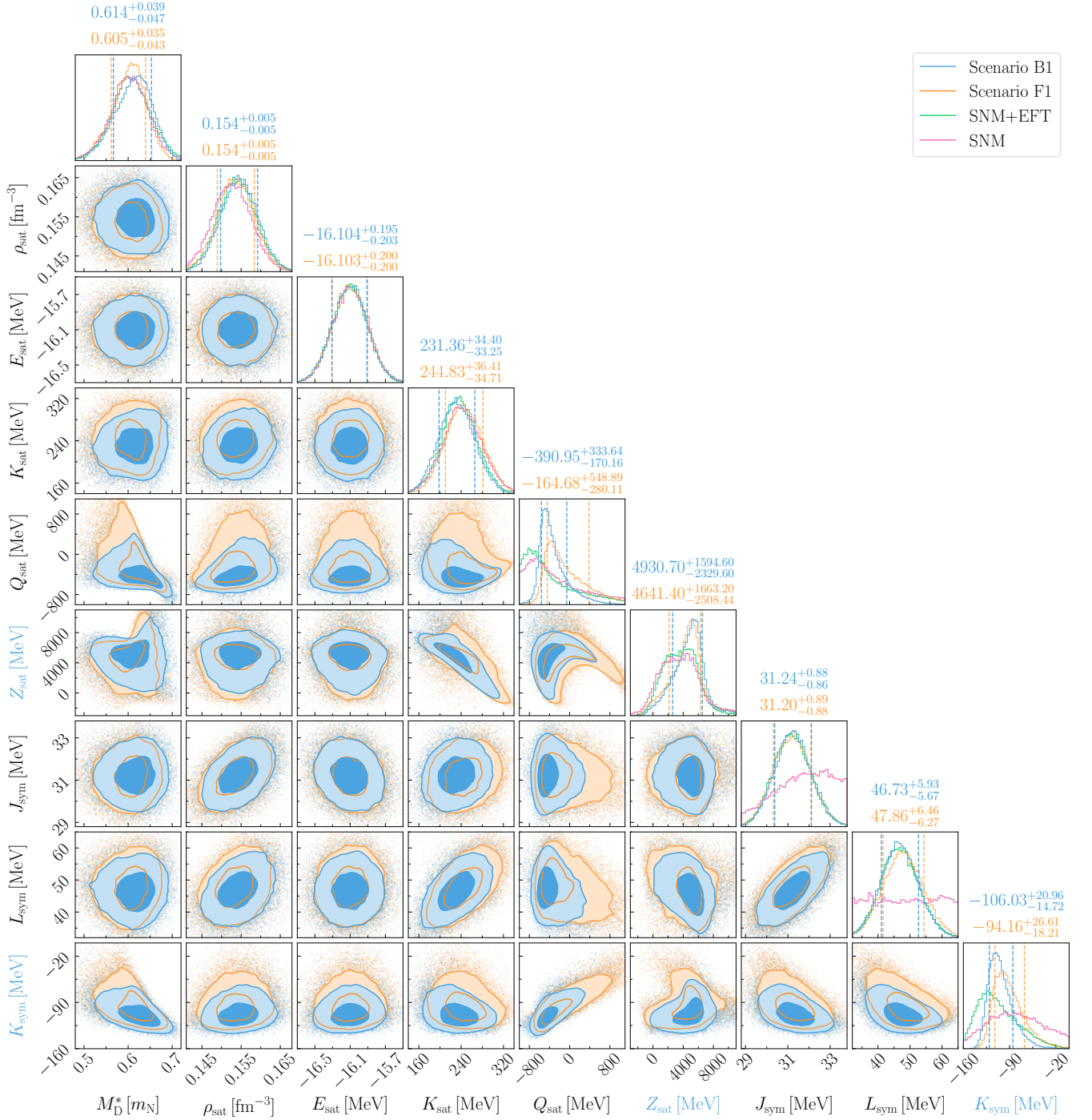


FIG. 12. Same as Fig. 11, but for nine nuclear characteristic parameters at saturation density. Note that the higher-order characteristic parameters Z_{sat} and K_{sym} marked in blue color are predictions of the CDF model, once the lower-order parameters are fixed.

From Fig. 12, we observe that the lowest-order parameters, E_{sat} and J_{sym} , remain nearly identical in both scenarios B1 and F1, indicating that astrophysical constraints have no impact on these quantities. In contrast, the higher-order parameters, Q_{sat} and K_{sym} , exhibit significant sensitivity to astrophysical constraints. However, the variation in K_{sym} within the present CDF framework arises primarily from slight rearrangements of the lower-order isovector parameters J_{sym} and L_{sym} .

Now, let us examine the correlations among CS properties. Figure 13 presents the posterior distributions for nine key properties of CSs, including the radius R and the squared sound speed $c_s^2 = dP/d\varepsilon$ at the center of stars with masses of 1.0, 1.4, and $2.0 M_\odot$, as well as for the maximum-mass M_{max} configuration, under scenarios B1 and F1. The value of c_s^2 characterizes the stiffness of the EoS at the stellar center while R reflects the overall stiffness of the EoS from the

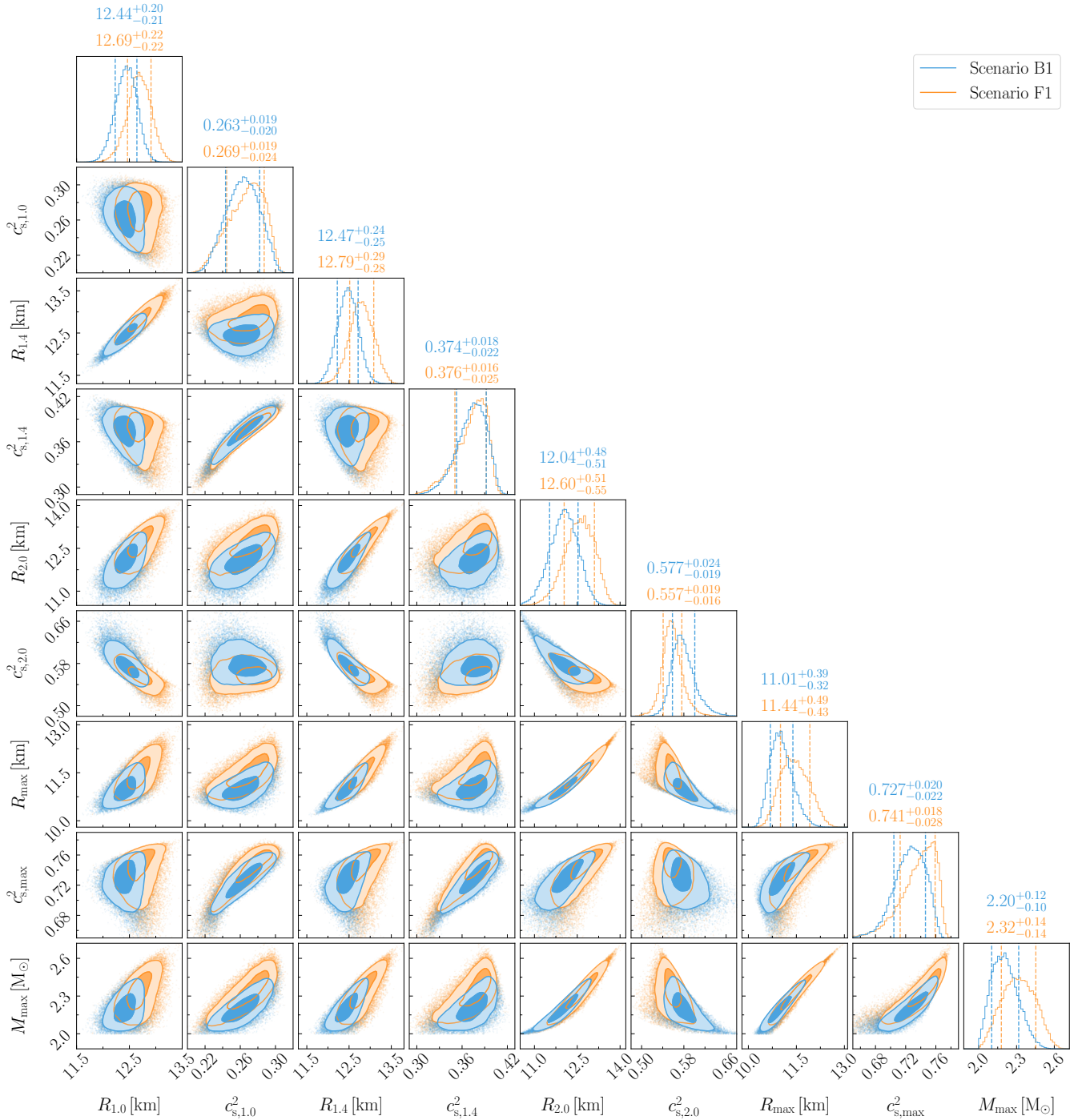


FIG. 13. Posterior distributions of nine gross properties of compact stars: radius R and sound speed c_s^2 at the center of the respective 1.0, 1.4, 2.0 M_\odot and the maximum-mass M_{\max} configurations, under astrophysical scenarios B1 and F1. The light and dark shaded regions indicate respectively the 68.3% and 95.4% CIs of the two-dimensional distributions, while the one-dimensional posteriors for each quantity are given at the edges of the plots where vertical lines indicate the 68.3% CI.

core to the surface. As shown in Fig. 13, the closer the masses of two stars, the stronger the correlation between their radii or central sound speeds. This trend is particularly evident for the present CDF-based EoS models, which exhibit a relatively straightforward behavior.

Finally we present in Fig. 14 the posterior correlation ma-

trix for variation of nuclear characteristic parameters at saturation density and selected gross properties of CSs under astrophysical scenarios B1 (in the lower-left) and F1 (in the upper-right). In this figure, we introduce also the dimensionless trace anomaly $\Delta = 1/3 - P/\varepsilon$ [127]. The correlations among nuclear matter characteristics are larger in their absolute values,

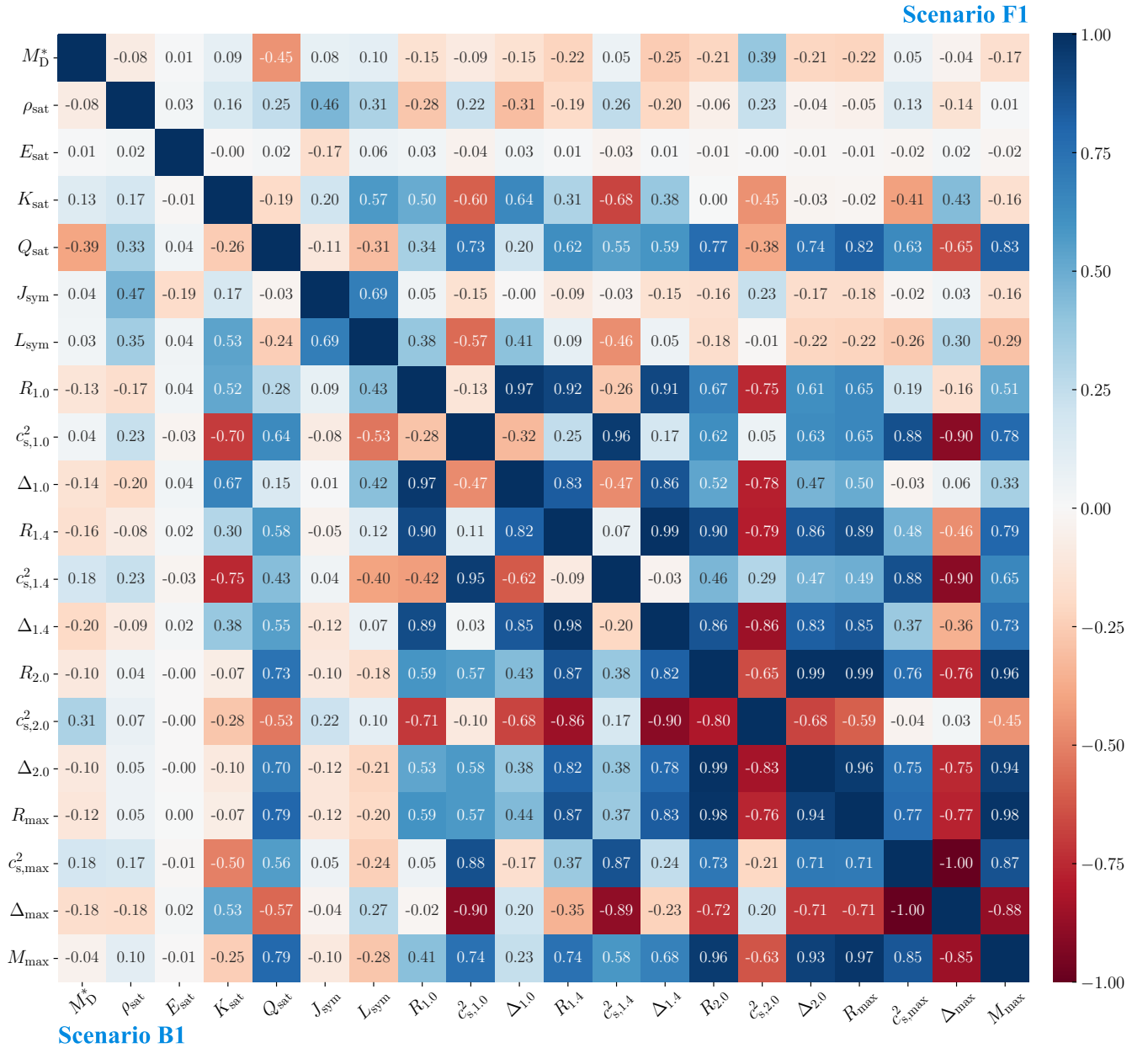


FIG. 14. Posterior correlation matrix for variation of nuclear characteristic parameters at saturation density and selected gross properties of compact stars under astrophysical scenarios B1 (lower-left part) and F1 (upper-right part).

compared to the case where only SNM constraints are applied in Fig. 2. In particular, the isovector pair $(J_{\text{sym}}, L_{\text{sym}})$ exhibits a strong correlation, with a Pearson coefficient of approximately $r \sim 0.7$. This correlation primarily arises from the χ EFT constraint on low-density PNM. The correlations among several key quantities of CSs are in agreement with our previous comments above. Finally, we emphasize once more that in our analysis, the isoscalar pair $(K_{\text{sat}}, Q_{\text{sat}})$ shows only a weak correlation ($r \sim 0.2$), whereas the pair $(K_{\text{sat}}, Z_{\text{sat}})$ exhibits a strong correlation (see Fig. 12). This behavior is qualitatively consistent with the findings of Ref. [22], where different observational constraints were employed. However, a recent study [32] reports a contrasting result: a strong cor-

relation between $(K_{\text{sat}}, Q_{\text{sat}})$ and an absence of correlation between $(K_{\text{sat}}, Z_{\text{sat}})$. Further work is required to understand the sensitivity of correlations to the modeling framework and the choice of constraints.

Correlations between nuclear characteristics and CS properties are encoded in the Pearson coefficients r . We find, notably, that the previously reported correlation between the slope of the symmetry energy L_{sym} and the radius of a $1.4 M_{\odot}$ star $R_{1,4}$ [95, 128–130], appears to have largely vanished, with $r \sim 0.1$, as also observed in Refs. [31, 131]. However, a moderate correlation remains between L_{sym} and the radius of a $1.0 M_{\odot}$ star - $R_{1,0}$, with a Pearson coefficient of approximately $r \sim 0.4$. It is important to note that the correlations reported

TABLE V. Characteristic parameters of symmetric nuclear matter at saturation density from the posterior distributions for scenarios B. The last column ($B_{1\text{ne}}$) corresponds to neglecting the χ EFT constraint. The superscripts and subscripts indicate the 68.3% and 95.4% (in parentheses) CI ranges.

Par.	Unit	Scenario B1	Scenario B2	Scenario B3	Scenario B4	Scenario $B_{1\text{ne}}$
M_D^*	m_N	$0.614^{+0.039(0.072)}_{-0.047(0.098)}$	$0.615^{+0.039(0.071)}_{-0.047(0.095)}$	$0.612^{+0.034(0.063)}_{-0.043(0.091)}$	$0.614^{+0.033(0.062)}_{-0.043(0.090)}$	$0.613^{+0.042(0.074)}_{-0.050(0.102)}$
ρ_{sat}	fm^{-3}	$0.154^{+0.005(0.009)}_{-0.005(0.009)}$	$0.155^{+0.005(0.010)}_{-0.005(0.009)}$	$0.155^{+0.005(0.009)}_{-0.005(0.009)}$	$0.155^{+0.005(0.009)}_{-0.005(0.009)}$	$0.154^{+0.005(0.010)}_{-0.005(0.010)}$
E_{sat}	MeV	$-16.10^{+0.20(0.40)}_{-0.20(0.40)}$	$-16.11^{+0.20(0.39)}_{-0.20(0.40)}$	$-16.11^{+0.20(0.40)}_{-0.20(0.40)}$	$-16.11^{+0.20(0.39)}_{-0.20(0.40)}$	$-16.09^{+0.20(0.39)}_{-0.20(0.40)}$
K_{sat}	MeV	$231.4^{+34.4(68.7)}_{-33.3(64.0)}$	$224.8^{+34.2(69.7)}_{-32.5(63.8)}$	$225.4^{+31.8(62.1)}_{-31.8(62.1)}$	$219.7^{+33.2(67.0)}_{-31.6(62.1)}$	$232.9^{+38.7(73.9)}_{-40.1(78.5)}$
Q_{sat}	MeV	$-391.0^{+333.6(872.8)}_{-170.2(323.3)}$	$-405.6^{+315.8(854.4)}_{-171.1(312.9)}$	$-215.0^{+435.7(994.7)}_{-253.0(437.5)}$	$-223.3^{+421.6(982.0)}_{-258.6(438.0)}$	$-386.9^{+369.1(1066.8)}_{-181.5(410.0)}$
Z_{sat}	MeV	$4931^{+1595(4862)}_{-2330(4721)}$	$5174^{+1477(4540)}_{-2170(4606)}$	$5393^{+1483(5424)}_{-1836(4413)}$	$5538^{+1433(5073)}_{-1712(4183)}$	$4944^{+2178(9408)}_{-2730(5259)}$
J_{sym}	MeV	$31.24^{+0.88(1.78)}_{-0.86(1.68)}$	$31.20^{+0.88(1.76)}_{-0.84(1.64)}$	$31.15^{+0.89(1.79)}_{-0.84(1.64)}$	$31.12^{+0.88(1.75)}_{-0.83(1.64)}$	$32.34^{+1.96(3.96)}_{-2.02(4.01)}$
L_{sym}	MeV	$46.73^{+5.94(12.10)}_{-5.67(11.35)}$	$45.73^{+5.64(11.79)}_{-5.59(11.29)}$	$45.46^{+5.86(12.08)}_{-5.79(11.20)}$	$44.45^{+5.79(11.89)}_{-5.65(11.21)}$	$45.03^{+14.46(27.35)}_{-13.62(23.80)}$
K_{sym}	MeV	$-106.0^{+21.0(50.5)}_{-14.7(25.8)}$	$-106.7^{+21.2(52.0)}_{-14.7(25.5)}$	$-96.8^{+24.0(58.3)}_{-16.6(28.8)}$	$-96.9^{+24.2(58.2)}_{-17.1(29.9)}$	$-104.6^{+35.3(83.9)}_{-25.7(48.5)}$
Q_{sym}	MeV	$776.1^{+155.5(295.8)}_{-159.1(323.0)}$	$802.6^{+149.4(288.2)}_{-151.1(312.5)}$	$836.6^{+147.0(265.3)}_{-155.6(318.7)}$	$864.3^{+139.8(256.3)}_{-152.9(317.0)}$	$856.2^{+368.7(676.0)}_{-381.7(682.4)}$
Z_{sym}	MeV	$-5079^{+1435(2523)}_{-1988(4606)}$	$-5225^{+1421(2496)}_{-1925(4585)}$	$-5979^{+1664(2927)}_{-2205(5025)}$	$-6155^{+1680(3188)}_{-2177(4910)}$	$-5965^{+3376(4990)}_{-4714(9446)}$

in Refs. [95, 128] were observed in a set of models where the isoscalar sector was nearly fixed and only the isovector parameters varied significantly.

V. CONCLUSIONS AND OUTLOOK

In this work, we extend the CDF-based Bayesian inference framework to incorporate the latest multi-messenger constraints, including NICER’s M - R estimates, gravitational wave events, and χ EFT computations. Additionally, we account for the heaviest known CS – the “black widow” pulsar PSR J0952-0607 – as well as the M - R estimates for the ultra-compact, low-mass object HESS J1731-347. We adopt the class of CDF models with linear mesonic terms and density-dependent meson-nucleon couplings, which have been extensively tested against various nuclear phenomena, allowing us to evaluate their flexibility and predictive power under more extreme astrophysical conditions.

A systematic analysis is performed for typical astrophysical scenarios where the importance of the individual impacts of PSR J0952-0607 and HESS J1731-347 are elucidated by assessing the posterior distributions for key properties of CSs, nuclear characteristics at saturation density, and correlations among them, and the density dependence of EoS and the symmetry energy.

We find that the present CDF models can naturally accommodate higher maximum masses for CSs, reaching values of approximately 2.4 - $2.5M_{\odot}$. This is accompanied by a noticeable increase in the radii of massive CSs by about 0.2 - 0.4 km. However, further softening of the low-density regime of the EoS to better match the HESS J1731-347 data appears challenging, likely requiring more refined modeling of the star itself, including phase transitions to quark matter, or further extensions of the CDF framework. Nevertheless, we imposed tighter limits on the parameter space of present CDF models which appear to be broadly consistent with current nuclear experimental and astrophysical data. We find that the two isovector parameters are tightly constrained at low-densities close to saturation, leaving little room for variation in the

high-density symmetry energy. As a result, the symmetry energy predicted by the CDF model is soft. Furthermore, the softness of the EoS at low densities suppresses the nucleonic direct Urca (DU) cooling process in CSs with $M \leq 2M_{\odot}$, as dictated by the behavior of the symmetry energy in the CDF model. A summary of the key predicted quantities for nuclear matter and CSs across various astrophysical scenarios is provided in the Appendix.

In conclusion, this work underscores the importance of combining multimessenger observations and advanced theoretical frameworks to enhance the fidelity of nuclear astrophysical models of CSs. The CDF models with density-dependent meson-nucleon couplings provide a robust theoretical framework to interpret currently known gross properties of CS. Due to the limited degrees of freedom in the isovector sector of the current CDF formulation, the predicted lower limit for the radii of low-mass stars cannot be reduced much below 12 km. Consequently, refining and extending the density dependence of CDF parameters is necessary to accurately model potential ultra-compact low-mass stars within the nucleonic paradigm. (Recall that a phase transition to quark matter may be an alternative solution as indicated above, see Refs. [45, 70] and references therein). Additional parameter(s) could also be useful within the CDF framework to provide greater control over the symmetry energy’s high-density behavior, particularly through the parameter K_{sym} . This issue will be further investigated in an upcoming study.

ACKNOWLEDGMENTS

J. J. L. and Y. T. acknowledge the support of the National Natural Science Foundation of China under Grants No. 12105232 and No. 12475150. A. S. acknowledges funding by the Deutsche Forschungsgemeinschaft Grant No. SE 1836/6-1 and the Polish NCN Grant No. 2023/51/B/ST9/02798.

TABLE VI. Key quantities of compact stars from the posterior distributions for scenarios B: radii, TDs, central baryonic densities, pressures, energy densities, sound speeds, and trace anomalies for 1.0, 1.4, 2.0 M_\odot and the maximum-mass M_{max} stars. We also list the inferred radius differences between 1.4, 2.0 M_\odot and 1.0, 1.4 M_\odot stars. The last column (B1_{ne}) corresponds to neglecting the χ EFT constraint. The superscripts and subscripts indicate the 68.3% and 95.4% (in parentheses) CI ranges.

Par.	Unit	Scenario B1	Scenario B2	Scenario B3	Scenario B4	Scenario B1 _{ne}
$R_{1.0}$	km	12.44 ^{+0.20(0.38)} -0.21(0.43)	12.36 ^{+0.21(0.40)} -0.22(0.42)	12.51 ^{+0.18(0.37)} -0.20(0.41)	12.44 ^{+0.20(0.38)} -0.21(0.41)	12.46 ^{+0.27(0.56)} -0.27(0.51)
$\Lambda_{1.0}$		3114 ⁺³³¹⁽⁶⁶⁷⁾ -323(619)	2999 ⁺³⁴⁶⁽⁶⁸³⁾ -319(596)	3259 ⁺³²¹⁽⁶⁷⁵⁾ -317(618)	3159 ⁺³⁴¹⁽⁶⁸³⁾ -320(614)	3176 ⁺³⁶³⁽⁷⁷⁶⁾ -341(653)
$\rho_{1.0}$	fm ⁻³	0.345 ^{+0.022(0.044)} -0.021(0.041)	0.348 ^{+0.023(0.045)} -0.022(0.042)	0.329 ^{+0.020(0.042)} -0.019(0.037)	0.333 ^{+0.021(0.044)} -0.020(0.039)	0.338 ^{+0.022(0.046)} -0.021(0.042)
$P_{1.0}$	MeV/fm ³	30.27 ^{+2.69(5.69)} -2.37(4.52)	31.07 ^{+2.86(5.84)} -2.56(4.81)	28.94 ^{+2.45(5.17)} -2.15(4.17)	29.56 ^{+2.62(5.51)} -2.31(4.41)	29.79 ^{+2.65(5.71)} -2.33(4.58)
$\epsilon_{1.0}$	MeV/fm ³	340.87 ^{+22.58(45.95)} -21.65(42.40)	346.57 ^{+23.87(47.02)} -22.41(44.03)	327.08 ^{+21.10(43.37)} -19.66(38.61)	331.63 ^{+22.21(45.91)} -20.49(40.26)	336.81 ^{+23.06(48.06)} -22.10(43.96)
$c_{s,1.0}^2$		0.263 ^{+0.019(0.033)} -0.020(0.037)	0.265 ^{+0.018(0.032)} -0.019(0.036)	0.274 ^{+0.016(0.026)} -0.018(0.037)	0.276 ^{+0.015(0.025)} -0.018(0.037)	0.264 ^{+0.027(0.047)} -0.026(0.047)
$\Delta_{1.0}$		0.244 ^{+0.002(0.004)} -0.002(0.005)	0.244 ^{+0.002(0.004)} -0.002(0.005)	0.245 ^{+0.002(0.004)} -0.002(0.004)	0.244 ^{+0.002(0.004)} -0.002(0.004)	0.245 ^{+0.003(0.006)} -0.003(0.005)
$R_{1.4}$	km	12.47 ^{+0.24(0.48)} -0.25(0.50)	12.39 ^{+0.26(0.49)} -0.26(0.50)	12.61 ^{+0.23(0.46)} -0.24(0.48)	12.54 ^{+0.24(0.47)} -0.25(0.50)	12.50 ^{+0.25(0.50)} -0.25(0.51)
$\Lambda_{1.4}$		472 ⁺⁷⁶⁽¹⁶³⁾ -65(121)	454 ⁺⁷⁵⁽¹⁶¹⁾ -65(118)	519 ⁺⁷⁶⁽¹⁶³⁾ -68(129)	503 ⁺⁷⁶⁽¹⁶⁴⁾ -69(130)	486 ⁺⁷⁸⁽¹⁷⁴⁾ -68(129)
$\rho_{1.4}$	fm ⁻³	0.425 ^{+0.036(0.070)} -0.035(0.067)	0.432 ^{+0.036(0.071)} -0.036(0.070)	0.400 ^{+0.033(0.067)} -0.030(0.057)	0.406 ^{+0.034(0.070)} -0.031(0.059)	0.419 ^{+0.038(0.075)} -0.037(0.071)
$P_{1.4}$	MeV/fm ³	60.04 ^{+7.485(15.313)} -6.823(12.859)	61.763 ^{+7.808(15.820)} -7.160(13.520)	55.432 ^{+6.564(13.889)} -5.778(10.937)	56.661 ^{+7.011(14.940)} -6.052(11.422)	58.872 ^{+7.696(16.131)} -7.017(13.282)
$\epsilon_{1.4}$	MeV/fm ³	433.76 ^{+39.20(76.56)} -38.65(73.38)	441.75 ^{+39.89(77.99)} -39.51(75.61)	406.84 ^{+35.26(72.82)} -33.54(61.79)	412.46 ^{+37.27(76.79)} -33.66(63.60)	427.67 ^{+42.64(83.86)} -41.19(77.86)
$c_{s,1.4}^2$		0.374 ^{+0.018(0.030)} -0.022(0.046)	0.377 ^{+0.017(0.029)} -0.020(0.044)	0.383 ^{+0.014(0.023)} -0.019(0.041)	0.385 ^{+0.013(0.022)} -0.018(0.040)	0.375 ^{+0.023(0.038)} -0.027(0.051)
$\Delta_{1.4}$		0.195 ^{+0.004(0.008)} -0.005(0.010)	0.193 ^{+0.005(0.009)} -0.005(0.010)	0.197 ^{+0.004(0.008)} -0.004(0.009)	0.196 ^{+0.004(0.008)} -0.005(0.010)	0.196 ^{+0.004(0.008)} -0.005(0.010)
$R_{2.0}$	km	12.04 ^{+0.48(0.91)} -0.51(1.03)	11.95 ^{+0.49(0.93)} -0.52(1.02)	12.38 ^{+0.40(0.77)} -0.45(0.92)	12.31 ^{+0.41(0.79)} -0.45(0.96)	12.11 ^{+0.49(0.95)} -0.55(1.11)
$\Lambda_{2.0}$		33.7 ^{+14.2(30.6)} -11.1(19.1)	31.1 ^{+13.6(29.7)} -10.5(17.7)	42.8 ^{+13.9(29.7)} -12.0(21.9)	40.9 ^{+13.7(29.3)} -11.9(21.2)	35.0 ^{+16.1(34.9)} -12.7(21.2)
$\rho_{2.0}$	fm ⁻³	0.636 ^{+0.122(0.273)} -0.093(0.162)	0.653 ^{+0.123(0.266)} -0.097(0.169)	0.568 ^{+0.088(0.205)} -0.067(0.120)	0.578 ^{+0.093(0.219)} -0.070(0.123)	0.623 ^{+0.134(0.291)} -0.099(0.169)
$P_{2.0}$	MeV/fm ³	193.66 ^{+72.30(185.95)} -46.59(76.50)	202.93 ^{+76.65(188.17)} -49.51(81.60)	158.85 ^{+45.43(118.10)} -30.66(62.38)	164.06 ^{+49.27(130.99)} -32.46(65.09)	186.18 ^{+79.54(199.82)} -47.67(77.15)
$\epsilon_{2.0}$	MeV/fm ³	704.78 ^{+164.86(385.85)} -118.38(201.48)	726.13 ^{+167.48(379.18)} -123.53(211.30)	617.12 ^{+112.83(273.48)} -82.44(145.17)	629.51 ^{+119.41(293.40)} -85.86(149.94)	687.99 ^{+181.32(411.07)} -125.32(208.97)
$c_{s,2.0}^2$		0.577 ^{+0.024(0.057)} -0.019(0.036)	0.582 ^{+0.025(0.059)} -0.020(0.038)	0.569 ^{+0.018(0.040)} -0.015(0.030)	0.572 ^{+0.019(0.040)} -0.016(0.031)	0.575 ^{+0.026(0.064)} -0.021(0.043)
$\Delta_{2.0}$		0.059 ^{+0.024(0.042)} -0.032(0.074)	0.054 ^{+0.025(0.044)} -0.033(0.075)	0.076 ^{+0.018(0.032)} -0.023(0.054)	0.073 ^{+0.019(0.032)} -0.025(0.059)	0.063 ^{+0.025(0.043)} -0.035(0.082)
M_{max}	M_\odot	2.20 ^{+0.12(0.23)} -0.10(0.17)	2.19 ^{+0.11(0.23)} -0.10(0.16)	2.28 ^{+0.10(0.20)} -0.10(0.19)	2.27 ^{+0.10(0.20)} -0.10(0.19)	2.21 ^{+0.13(0.26)} -0.11(0.19)
$R_{M_{\text{max}}}$	km	11.00 ^{+0.39(0.80)} -0.32(0.58)	10.94 ^{+0.38(0.79)} -0.32(0.57)	11.27 ^{+0.36(0.73)} -0.34(0.63)	11.22 ^{+0.36(0.74)} -0.34(0.64)	11.05 ^{+0.42(0.88)} -0.35(0.62)
$\Lambda_{M_{\text{max}}}$		6.04 ^{+0.78(1.78)} -0.58(0.93)	6.05 ^{+0.69(1.59)} -0.56(0.91)	5.64 ^{+0.61(1.45)} -0.40(0.64)	5.64 ^{+0.57(1.36)} -0.39(0.61)	6.02 ^{+0.91(2.05)} -0.68(1.02)
$\rho_{M_{\text{max}}}$	fm ⁻³	0.996 ^{+0.075(0.136)} -0.079(0.152)	1.008 ^{+0.073(0.132)} -0.079(0.153)	0.939 ^{+0.070(0.139)} -0.066(0.127)	0.948 ^{+0.072(0.142)} -0.068(0.128)	0.986 ^{+0.083(0.148)} -0.088(0.166)
$P_{M_{\text{max}}}$	MeV/fm ³	588.95 ^{+30.94(62.09)} -31.28(62.70)	596.25 ^{+32.32(62.72)} -31.84(64.58)	569.79 ^{+29.69(60.19)} -29.47(58.40)	575.54 ^{+30.96(62.88)} -30.51(60.15)	582.77 ^{+36.75(74.48)} -35.70(68.17)
$\epsilon_{M_{\text{max}}}$	MeV/fm ³	1298.90 ^{+97.16(177.49)} -104.00(199.98)	1315.11 ^{+95.49(174.06)} -103.93(201.79)	1224.77 ^{+89.22(181.76)} -89.22(167.09)	1236.73 ^{+94.77(186.52)} -89.22(169.07)	1285.11 ^{+110.22(198.89)} -115.70(218.44)
$c_{s,M_{\text{max}}}^2$		0.726 ^{+0.020(0.032)} -0.023(0.049)	0.726 ^{+0.019(0.032)} -0.020(0.044)	0.740 ^{+0.014(0.023)} -0.019(0.043)	0.739 ^{+0.014(0.023)} -0.018(0.040)	0.728 ^{+0.022(0.034)} -0.026(0.057)
$\Delta_{M_{\text{max}}}$		-0.123 ^{+0.018(0.038)} -0.016(0.027)	-0.123 ^{+0.016(0.035)} -0.015(0.026)	-0.134 ^{+0.016(0.035)} -0.012(0.019)	-0.134 ^{+0.015(0.033)} -0.011(0.019)	-0.124 ^{+0.021(0.044)} -0.019(0.029)
$R_{1.4}-R_{2.0}$	km	0.41 ^{+0.34(0.74)} -0.27(0.46)	0.43 ^{+0.33(0.71)} -0.27(0.47)	0.21 ^{+0.25(0.58)} -0.19(0.34)	0.22 ^{+0.26(0.59)} -0.19(0.34)	0.37 ^{+0.42(0.87)} -0.33(0.54)
$R_{1.4}-R_{1.0}$	km	0.03 ^{+0.11(0.21)} -0.11(0.20)	0.03 ^{+0.11(0.21)} -0.10(0.20)	0.11 ^{+0.10(0.18)} -0.10(0.20)	0.10 ^{+0.09(0.18)} -0.10(0.20)	0.05 ^{+0.16(0.28)} -0.19(0.37)

TABLE VII. The same as Table V, but for scenarios F.

Par.	Unit	Scenario F1	Scenario F2	Scenario F3	Scenario F4	Scenario F1 _{ne}
M_D^*	m_N	0.605 ^{+0.035(0.070)} -0.043(0.091)	0.606 ^{+0.036(0.070)} -0.043(0.092)	0.601 ^{+0.030(0.059)} -0.039(0.086)	0.603 ^{+0.030(0.060)} -0.039(0.086)	0.607 ^{+0.041(0.075)} -0.047(0.098)
ρ_{sat}	fm ⁻³	0.154 ^{+0.005(0.009)} -0.005(0.009)	0.154 ^{+0.005(0.009)} -0.005(0.009)	0.154 ^{+0.005(0.009)} -0.005(0.009)	0.154 ^{+0.005(0.009)} -0.004(0.009)	0.153 ^{+0.005(0.010)} -0.005(0.010)
E_{sat}	MeV	-16.10 ^{+0.20(0.40)} -0.20(0.40)	-16.10 ^{+0.20(0.40)} -0.20(0.40)	-16.11 ^{+0.20(0.40)} -0.19(0.39)	-16.11 ^{+0.20(0.40)} -0.20(0.40)	-16.09 ^{+0.20(0.40)} -0.20(0.40)
K_{sat}	MeV	244.8 ^{+36.4(71.2)} -34.7(67.8)	236.9 ^{+36.8(73.6)} -34.1(66.4)	241.2 ^{+33.7(70.3)} -32.7(63.8)	234.0 ^{+33.9(69.9)} -32.4(63.3)	240.2 ^{+40.9(78.0)} -40.1(79.8)
Q_{sat}	MeV	-164.7 ^{+548.9(1161.9)} -280.1(455.4)	-195.8 ^{+544.8(1163.0)} -271.8(444.7)	81.0 ^{+548.4(1071.4)} -386.6(625.9)	47.1 ^{+540.6(1069.8)} -375.9(604.3)	-285.5 ^{+560.4(1340.1)} -244.6(476.7)
Z_{sat}	MeV	4641 ⁺¹⁶⁶³⁽⁵⁴⁹⁷⁾ -2508(5071)	4872 ⁺¹⁶²³⁽⁵³⁸¹⁾ -2314(5105)	4877 ⁺¹⁷⁹⁶⁽⁵⁷²⁹⁾ -1928(4831)	5053 ⁺¹⁶⁷⁴⁽⁵⁴³⁷⁾ -1957(4790)	4707 ⁺²⁴⁵²⁽¹²⁸⁶⁾ -2916(5468)
J_{sym}	MeV	31.20 ^{+0.89(1.82)} -0.88(1.72)	31.15 ^{+0.91(1.83)} -0.85(1.69)	31.12 ^{+0.88(1.79)} -0.86(1.70)	31.05 ^{+0.88(1.78)} -0.84(1.65)	32.25 ^{+2.03(4.00)} -2.03(3.99)
L_{sym}	MeV	47.86 ^{+6.46(13.08)} -6.27(12.15)	46.62 ^{+6.36(13.00)} -6.14(11.97)	46.75 ^{+6.38(13.15)} -6.12(11.87)	45.46 ^{+6.22(12.77)} -6.02(11.62)	64.03 ^{+16.66(28.09)} -21.16(37.18)
K_{sym}	MeV	-94.2 ^{+26.6(61.8)} -18.2(31.1)	-95.1 ^{+27.5(62.3)} -18.3(31.6)	-83.8 ^{+26.9(60.7)} -19.5(34.1)	-84.1 ^{+27.9(60.7)} -20.1(35.3)	-83.3 ^{+39.4(78.9)} -30.4(55.5)
Q_{sym}	MeV	765.3 ^{+166.5(299.3)} -177.0(358.4)	796.9 ^{+161.8(290.8)} -174.7(354.3)	817.7 ^{+145.1(263.3)} -166.5(347.3)	847.2 ^{+141.3(257.0)} -163.1(340.3)	389.6 ^{+550.8(997.8)} -339.0(565.2)
Z_{sym}	MeV	-5686 ⁺¹⁸²⁰⁽³⁰⁹⁵⁾ -2596(5565)	-5853 ⁺¹⁸³⁵⁽³¹¹⁹⁾ -2566(5491)	-6702 ⁺²⁰²⁴⁽³⁵⁰⁸⁾ -2563(5287)	-6857 ⁺²⁰²²⁽³⁵³⁸⁾ -2577(5323)	-2740 ⁺¹⁸⁹¹⁽²⁸⁰⁸⁾ -5076(11484)

Appendix: Key quantities of nuclear matter and compact stars

In this appendix, we present the characteristic parameters of nuclear matter at saturation density and key gross quantities of CSs predicted by CDFs under different astrophysical

scenarios. The results obtained from Scenarios B are listed in Tables V and VI, and those from Scenarios F in Tables VII and VIII.

To ensure the presentation is self-contained, we give here the definitions for nuclear matter characteristic coefficients.

TABLE VIII. The same as Table VI, but for scenarios F.

Par.	Unit	Scenario F1	Scenario F2	Scenario F3	Scenario F4	Scenario F1 _{ne}
$R_{1,0}$	km	12.69 ^{+0.22(0.43)} -0.22(0.47)	12.61 ^{+0.22(0.43)} -0.25(0.50)	12.75 ^{+0.21(0.41)} -0.21(0.44)	12.68 ^{+0.21(0.40)} -0.22(0.45)	13.05 ^{+0.44(0.75)} -0.44(0.81)
$\Lambda_{1,0}$		3554 ⁺⁴²⁹⁽⁸⁵⁸⁾ -388(764)	3429 ⁺⁴⁰⁵⁽⁸²²⁾ -412(790)	3712 ⁺⁴¹³⁽⁷⁹⁹⁾ -383(740)	3584 ⁺⁴⁰¹⁽⁷⁷³⁾ -376(736)	4046 ⁺⁷⁵⁶⁽¹⁴⁶⁵⁾ -622(1104)
$\rho_{1,0}$	fm ⁻³	0.316 ^{+0.023(0.047)} -0.022(0.040)	0.322 ^{+0.024(0.051)} -0.023(0.042)	0.304 ^{+0.021(0.043)} -0.019(0.033)	0.310 ^{+0.022(0.044)} -0.019(0.033)	0.308 ^{+0.023(0.047)} -0.021(0.036)
$P_{1,0}$	MeV/fm ³	27.19 ^{+2.66(5.69)} -2.46(4.43)	27.94 ^{+2.93(6.31)} -2.52(4.61)	26.06 ^{+2.41(5.03)} -2.13(3.77)	26.70 ^{+2.51(5.31)} -2.14(3.80)	25.46 ^{+2.99(6.11)} -2.54(4.46)
$\epsilon_{1,0}$	MeV/fm ³	313.91 ^{+23.82(48.94)} -23.39(41.88)	319.79 ^{+25.06(52.72)} -23.93(43.46)	301.73 ^{+21.78(44.24)} -19.38(34.30)	307.07 ^{+22.21(45.92)} -19.64(34.55)	306.92 ^{+23.90(48.44)} -21.29(37.60)
$c_{s,1,0}^2$		0.269 ^{+0.019(0.030)} -0.024(0.044)	0.271 ^{+0.018(0.029)} -0.023(0.044)	0.278 ^{+0.014(0.023)} -0.019(0.041)	0.279 ^{+0.013(0.022)} -0.018(0.040)	0.242 ^{+0.039(0.065)} -0.037(0.060)
$\Delta_{1,0}$		0.247 ^{+0.002(0.005)} -0.002(0.005)	0.246 ^{+0.002(0.005)} -0.002(0.005)	0.247 ^{+0.002(0.004)} -0.002(0.004)	0.246 ^{+0.002(0.004)} -0.002(0.004)	0.250 ^{+0.005(0.008)} -0.004(0.007)
$R_{1,4}$	km	12.79 ^{+0.29(0.55)} -0.28(0.56)	12.71 ^{+0.28(0.54)} -0.30(0.60)	12.93 ^{+0.26(0.48)} -0.27(0.53)	12.85 ^{+0.26(0.48)} -0.27(0.54)	13.01 ^{+0.34(0.60)} -0.34(0.67)
$\Lambda_{1,4}$		571 ⁺¹⁰⁶⁽²⁰⁷⁾ -87(162)	547 ⁺¹⁰¹⁽²⁰³⁾ -87(163)	622 ⁺⁹⁶⁽¹⁸⁵⁾ -89(164)	598 ⁺⁹¹⁽¹⁷⁴⁾ -87(162)	610 ⁺¹⁰⁹⁽²¹²⁾ -97(176)
$\rho_{1,4}$	fm ⁻³	0.384 ^{+0.039(0.078)} -0.036(0.062)	0.392 ^{+0.039(0.080)} -0.038(0.065)	0.364 ^{+0.033(0.068)} -0.028(0.048)	0.371 ^{+0.033(0.069)} -0.029(0.049)	0.387 ^{+0.039(0.075)} -0.037(0.065)
$P_{1,4}$	MeV/fm ³	51.927 ^{+7.378(15.549)} -6.725(11.458)	53.504 ^{+7.822(16.897)} -6.910(12.027)	48.216 ^{+6.288(13.259)} -5.196(8.919)	49.616 ^{+6.508(13.863)} -5.327(9.099)	51.114 ^{+7.346(15.012)} -6.310(11.027)
$\epsilon_{1,4}$	MeV/fm ³	389.96 ^{+42.17(85.26)} -39.23(66.82)	398.48 ^{+43.12(87.93)} -40.73(69.93)	367.88 ^{+35.52(73.68)} -30.02(51.54)	375.12 ^{+36.16(74.78)} -30.77(52.47)	394.15 ^{+43.01(82.13)} -40.79(70.56)
$c_{s,1,4}^2$		0.376 ^{+0.016(0.026)} -0.025(0.054)	0.378 ^{+0.016(0.025)} -0.023(0.053)	0.383 ^{+0.012(0.019)} -0.019(0.045)	0.385 ^{+0.012(0.019)} -0.018(0.043)	0.354 ^{+0.033(0.052)} -0.036(0.067)
$\Delta_{1,4}$		0.200 ^{+0.004(0.008)} -0.005(0.010)	0.199 ^{+0.005(0.008)} -0.005(0.011)	0.202 ^{+0.004(0.007)} -0.004(0.009)	0.201 ^{+0.004(0.007)} -0.004(0.009)	0.203 ^{+0.005(0.009)} -0.006(0.011)
$R_{2,0}$	km	12.60 ^{+0.51(0.88)} -0.55(1.14)	12.49 ^{+0.51(0.91)} -0.55(1.14)	12.88 ^{+0.39(0.70)} -0.45(0.94)	12.78 ^{+0.39(0.69)} -0.45(0.95)	12.58 ^{+0.54(0.95)} -0.60(1.20)
$\Lambda_{2,0}$		48.9 ^{+20.1(38.6)} -16.5(28.6)	45.0 ^{+19.4(37.9)} -15.4(26.9)	59.6 ^{+17.5(33.3)} -16.0(29.6)	56.2 ^{+16.8(31.6)} -15.3(28.1)	45.8 ^{+21.8(42.0)} -17.2(28.3)
$\rho_{2,0}$	fm ⁻³	0.539 ^{+0.110(0.254)} -0.078(0.126)	0.555 ^{+0.113(0.260)} -0.082(0.133)	0.492 ^{+0.075(0.177)} -0.054(0.090)	0.505 ^{+0.078(0.182)} -0.057(0.092)	0.565 ^{+0.134(0.292)} -0.095(0.149)
$P_{2,0}$	MeV/fm ³	144.69 ^{+54.57(143.77)} -33.64(51.71)	152.24 ^{+57.61(152.18)} -36.25(56.25)	124.22 ^{+33.65(86.56)} -23.00(35.18)	129.65 ^{+35.82(91.55)} -23.45(37.17)	155.65 ^{+70.83(178.64)} -41.29(62.01)
$\epsilon_{2,0}$	MeV/fm ³	582.67 ^{+140.79(339.60)} -95.26(150.38)	601.98 ^{+144.60(348.88)} -100.50(160.27)	525.43 ^{+92.48(225.36)} -64.55(105.20)	539.74 ^{+96.25(232.28)} -67.98(109.20)	617.46 ^{+178.13(401.64)} -118.56(182.19)
$c_{s,2,0}^2$		0.557 ^{+0.019(0.045)} -0.016(0.036)	0.562 ^{+0.021(0.050)} -0.017(0.035)	0.554 ^{+0.015(0.033)} -0.014(0.030)	0.557 ^{+0.015(0.035)} -0.014(0.029)	0.555 ^{+0.023(0.057)} -0.021(0.045)
$\Delta_{2,0}$		0.085 ^{+0.020(0.033)} -0.027(0.065)	0.081 ^{+0.022(0.035)} -0.028(0.068)	0.097 ^{+0.015(0.025)} -0.019(0.045)	0.093 ^{+0.015(0.025)} -0.020(0.047)	0.081 ^{+0.023(0.037)} -0.033(0.077)
M_{\max}	M_{\odot}	2.37 ^{+0.14(0.24)} -0.14(0.24)	2.30 ^{+0.14(0.24)} -0.13(0.23)	2.39 ^{+0.11(0.19)} -0.12(0.23)	2.37 ^{+0.11(0.19)} -0.12(0.22)	2.27 ^{+0.16(0.28)} -0.14(0.23)
$R_{M_{\max}}$	km	11.44 ^{+0.49(0.88)} -0.43(0.78)	11.35 ^{+0.48(0.89)} -0.42(0.76)	11.70 ^{+0.40(0.71)} -0.40(0.77)	11.62 ^{+0.39(0.70)} -0.40(0.75)	11.37 ^{+0.50(0.93)} -0.41(0.70)
$\Lambda_{M_{\max}}$		5.64 ^{+0.89(2.18)} -0.51(0.73)	5.67 ^{+0.81(2.02)} -0.50(0.74)	5.34 ^{+0.56(1.52)} -0.31(0.48)	5.36 ^{+0.55(1.43)} -0.31(0.48)	6.04 ^{+1.24(2.67)} -0.81(1.14)
$\rho_{M_{\max}}$	fm ⁻³	0.912 ^{+0.091(0.169)} -0.084(0.142)	0.928 ^{+0.089(0.166)} -0.086(0.147)	0.864 ^{+0.074(0.152)} -0.063(0.108)	0.877 ^{+0.075(0.151)} -0.065(0.109)	0.935 ^{+0.094(0.162)} -0.096(0.162)
$P_{M_{\max}}$	MeV/fm ³	551.63 ^{+34.92(69.28)} -34.96(63.29)	559.77 ^{+35.43(72.67)} -35.57(66.13)	534.23 ^{+32.30(64.15)} -30.03(53.29)	541.30 ^{+32.07(65.21)} -30.83(54.22)	554.04 ^{+36.80(71.19)} -35.56(65.38)
$\epsilon_{M_{\max}}$	MeV/fm ³	1189.94 ^{+116.94(219.07)} -111.16(188.08)	1209.51 ^{+114.86(216.09)} -112.67(194.16)	1126.41 ^{+97.23(198.06)} -83.56(142.85)	1143.10 ^{+98.06(196.78)} -85.54(144.32)	1222.63 ^{+123.06(214.00)} -128.27(216.29)
$c_{s,M_{\max}}^2$		0.741 ^{+0.018(0.028)} -0.028(0.063)	0.739 ^{+0.018(0.028)} -0.025(0.058)	0.751 ^{+0.012(0.019)} -0.019(0.048)	0.750 ^{+0.012(0.019)} -0.019(0.045)	0.732 ^{+0.026(0.038)} -0.034(0.068)
$\Delta_{M_{\max}}$		-0.134 ^{+0.022(0.049)} -0.015(0.023)	-0.133 ^{+0.020(0.046)} -0.015(0.023)	-0.143 ^{+0.016(0.039)} -0.010(0.015)	-0.142 ^{+0.016(0.036)} -0.010(0.015)	-0.125 ^{+0.027(0.053)} -0.022(0.032)
$R_{1,4}-R_{2,0}$	km	0.18 ^{+0.34(0.75)} -0.23(0.37)	0.20 ^{+0.33(0.74)} -0.24(0.39)	0.04 ^{+0.22(0.53)} -0.16(0.27)	0.06 ^{+0.23(0.54)} -0.16(0.27)	0.40 ^{+0.52(1.07)} -0.38(0.61)
$R_{1,4}-R_{1,0}$	km	0.12 ^{+0.12(0.20)} -0.13(0.24)	0.11 ^{+0.12(0.21)} -0.12(0.23)	0.18 ^{+0.09(0.16)} -0.10(0.21)	0.17 ^{+0.09(0.16)} -0.10(0.21)	-0.03 ^{+0.23(0.38)} -0.23(0.41)

For the isoscalar sector, an order n coefficient can be defined as

$$X_{\text{sat}}^n = 3^n \rho_{\text{sat}}^n \left. \frac{\partial^n \varepsilon(\rho, 0)}{\partial \rho^n} \right|_{\rho_{\text{sat}}}, \quad (\text{A.1})$$

where $\varepsilon(\rho, 0)$ is the energy density of symmetric matter. It gives at saturation density the energy per nucleon E_{sat} ($n = 0$), the incompressibility K_{sat} ($n = 2$), the skewness Q_{sat} ($n = 3$), and the kurtosis Z_{sat} ($n = 4$), respectively. For the the isovector sector, the symmetry energy is computed from

$$E_{\text{sym}}(\rho) = \frac{1}{2} \left. \frac{\partial^n \varepsilon(\rho, \delta)}{\partial \delta^2} \right|_{\delta=0}. \quad (\text{A.2})$$

Similarly, it can be expanded close to the saturation density

and an order n coefficient can be written as

$$X_{\text{sym}}^n = 3^n \rho_{\text{sat}}^n \left. \frac{\partial^n E_{\text{sym}}(\rho)}{\partial \rho^n} \right|_{\rho_{\text{sat}}}, \quad (\text{A.3})$$

with J_{sym} ($n = 0$) the symmetry energy coefficient at saturation density, the slope L_{sym} ($n = 1$), the curvature K_{sym} ($n = 2$), the skewness Q_{sym} ($n = 3$), and the kurtosis Z_{sym} ($n = 4$), respectively.

Note that in Tables V and VII we also show the values of higher order parameters Z_{sat} in the isoscalar sector and K_{sym} , Q_{sym} and Z_{sym} in the isovector sector, which are predictions based on values of the lower-order parameters that fix the parameters of the present CDF.

[1] G. Raaijmakers, T. E. Riley, A. L. Watts, *et al.*, A *NICER* view of PSR J0030+0451: Implications for the dense matter equation of state, *Astrophys. J. Lett.* **887**, L22 (2019),

arXiv:1912.05703 [astro-ph.HE].

[2] P. Landry, R. Essick, and K. Chatzioannou, Nonparametric constraints on neutron star matter with existing and upcoming

- gravitational wave and pulsar observations, *Phys. Rev. D* **101**, 123007 (2020), [arXiv:2003.04880 \[astro-ph.HE\]](#).
- [3] G. Raaijmakers, S. K. Greif, T. E. Riley, *et al.*, Constraining the dense matter equation of state with joint analysis of NICER and LIGO/Virgo measurements, *Astrophys. J. Lett.* **893**, L21 (2020), [arXiv:1912.11031 \[astro-ph.HE\]](#).
- [4] I. Legred, K. Chatziioannou, R. Essick, S. Han, and P. Landry, Impact of the PSR J0740+6620 radius constraint on the properties of high-density matter, *Phys. Rev. D* **104**, 063003 (2021), [arXiv:2106.05313 \[astro-ph.HE\]](#).
- [5] P. T. H. Pang, I. Tews, M. W. Coughlin, *et al.*, Nuclear Physics Multimessenger Astrophysics Constraints on the Neutron Star Equation of State: Adding NICER’s PSR J0740+6620 Measurement, *Astrophys. J.* **922**, 14 (2021), [arXiv:2105.08688 \[astro-ph.HE\]](#).
- [6] S. Altiparmak, C. Ecker, and L. Rezzolla, On the Sound Speed in Neutron Stars, *Astrophys. J. Lett.* **939**, L34 (2022), [arXiv:2203.14974 \[astro-ph.HE\]](#).
- [7] E. Annala, T. Gorda, E. Katerini, A. Kurkela, J. Nättilä, V. Paschalidis, and A. Vuorinen, Multimessenger Constraints for Ultradense Matter, *Phys. Rev. X* **12**, 011058 (2022), [arXiv:2105.05132 \[astro-ph.HE\]](#).
- [8] E. Annala, T. Gorda, J. Hirvonen, O. Komoltsev, A. Kurkela, J. Nättilä, and A. Vuorinen, Strongly interacting matter exhibits deconfined behavior in massive neutron stars, *Nat. Commun.* **14**, 8451 (2023), [arXiv:2303.11356 \[astro-ph.HE\]](#).
- [9] E. V. Chimanski, R. V. Lobato, A. R. Goncalves, and C. A. Bertulani, Bayesian Exploration of Phenomenological EoS of Neutron/Hybrid Stars with Recent Observations, *Parti.* **6**, 198 (2023), [arXiv:2205.01174 \[nucl-th\]](#).
- [10] N. Rutherford, M. Mendes, I. Svensson, *et al.*, Constraining the Dense Matter Equation of State with New NICER Mass–Radius Measurements and New Chiral Effective Field Theory Inputs, *Astrophys. J. Lett.* **971**, L19 (2024), [arXiv:2407.06790 \[astro-ph.HE\]](#).
- [11] Y.-Z. Fan, M.-Z. Han, J.-L. Jiang, D.-S. Shao, and S.-P. Tang, Maximum gravitational mass $M_{\text{TOV}} = 2.25_{-0.07}^{+0.08} M_{\odot}$ inferred at about 3% precision with multimessenger data of neutron stars, *Phys. Rev. D* **109**, 043052 (2024), [arXiv:2309.12644 \[astro-ph.HE\]](#).
- [12] C. Mondal and F. Gulminelli, Nucleonic metamodelling in light of multimessenger, PREX-II, and CREX data, *Phys. Rev. C* **107**, 015801 (2023), [arXiv:2209.05177 \[nucl-th\]](#).
- [13] J. Zhou, J. Xu, and P. Papakonstantinou, Bayesian inference of neutron-star observables based on effective nuclear interactions, *Phys. Rev. C* **107**, 055803 (2023), [arXiv:2301.07904 \[nucl-th\]](#).
- [14] M. V. Beznogov and A. R. Raduta, Bayesian Survey of the Dense Matter Equation of State Built upon Skyrme Effective Interactions, *Astrophys. J.* **966**, 216 (2024), [arXiv:2308.15351 \[astro-ph.HE\]](#).
- [15] M. V. Beznogov and A. R. Raduta, Bayesian inference of the dense matter equation of state built upon extended Skyrme interactions, *Phys. Rev. C* **110**, 035805 (2024), [arXiv:2403.19325 \[nucl-th\]](#).
- [16] C. Y. Tsang, M. B. Tsang, W. G. Lynch, R. Kumar, and C. J. Horowitz, Determination of the equation of state from nuclear experiments and neutron star observations, *Nature Astron.* **8**, 328 (2024), [arXiv:2310.11588 \[nucl-th\]](#).
- [17] S. Traversi, P. Char, and G. Pagliara, Bayesian Inference of Dense Matter Equation of State within Relativistic Mean Field Models using Astrophysical Measurements, *Astrophys. J.* **897**, 165 (2020), [arXiv:2002.08951 \[astro-ph.HE\]](#).
- [18] T. Malik, M. Ferreira, B. K. Agrawal, and C. Providência, Relativistic Description of Dense Matter Equation of State and Compatibility with Neutron Star Observables: A Bayesian Approach, *Astrophys. J.* **930**, 17 (2022), [arXiv:2201.12552 \[nucl-th\]](#).
- [19] T. Malik, B. K. Agrawal, and C. Providência, Inferring the nuclear symmetry energy at suprasaturation density from neutrino cooling, *Phys. Rev. C* **106**, L042801 (2022), [arXiv:2206.15404 \[nucl-th\]](#).
- [20] X. Sun, Z. Miao, B. Sun, and A. Li, Astrophysical Implications on Hyperon Couplings and Hyperon Star Properties with Relativistic Equations of States, *Astrophys. J.* **942**, 55 (2023), [arXiv:2205.10631 \[astro-ph.HE\]](#).
- [21] Z. Zhu, A. Li, and T. Liu, A Bayesian Inference of a Relativistic Mean-field Model of Neutron Star Matter from Observations of NICER and GW170817/AT2017gfo, *Astrophys. J.* **943**, 163 (2023), [arXiv:2211.02007 \[astro-ph.HE\]](#).
- [22] C. Providência, T. Malik, M. B. Albino, and M. Ferreira, Neutron star equation of state: identifying hadronic matter characteristics, [arXiv](#), 2307.05086 (2023), [arXiv:2307.05086 \[nucl-th\]](#).
- [23] P. Char, C. Mondal, F. Gulminelli, and M. Oertel, Generalized description of neutron star matter with a nucleonic relativistic density functional, *Phys. Rev. D* **108**, 103045 (2023), [arXiv:2307.12364 \[nucl-th\]](#).
- [24] M. V. Beznogov and A. R. Raduta, Bayesian inference of the dense matter equation of state built upon covariant density functionals, *Phys. Rev. C* **107**, 045803 (2023), [arXiv:2212.07168 \[nucl-th\]](#).
- [25] T. Malik, M. Ferreira, M. B. Albino, and C. Providência, Spanning the full range of neutron star properties within a microscopic description, *Phys. Rev. D* **107**, 103018 (2023), [arXiv:2301.08169 \[nucl-th\]](#).
- [26] M. Salinas and J. Piekarewicz, Bayesian refinement of covariant energy density functionals, *Phys. Rev. C* **107**, 045802 (2023), [arXiv:2301.09692 \[nucl-th\]](#).
- [27] C. Huang, G. Raaijmakers, A. L. Watts, L. Tolos, and C. Providência, Constraining a relativistic mean field model using neutron star mass–radius measurements I: nucleonic models, *Mon. Not. R. Astron. Soc.* **529**, 4650 (2024), [arXiv:2303.17518 \[astro-ph.HE\]](#).
- [28] V. Parmar, V. B. Thapa, A. Kumar, D. Bandyopadhyay, and M. Sinha, Bayesian inference of the dense-matter equation of state of neutron stars with antikaon condensation, *Phys. Rev. C* **110**, 045804 (2024), [arXiv:2409.19451 \[astro-ph.HE\]](#).
- [29] L. Scurto, H. Pais, and F. Gulminelli, General predictions of neutron star properties using unified relativistic mean-field equations of state, *Phys. Rev. D* **109**, 103015 (2024), [arXiv:2402.15548 \[nucl-th\]](#).
- [30] S. Tewari, S. Chatterjee, D. Kumar, and R. Mallick, Analyzing the dense matter equation of states in the light of the compact object HESS J1731–347, [arXiv](#), 2410.20355 (2024), [arXiv:2410.20355 \[astro-ph.HE\]](#).
- [31] J.-J. Li, Y. Tian, and A. Sedrakian, Bayesian Constraints on Covariant Density Functional Equations of State of Compact Stars with New NICER Mass-Radius Measurements, [arXiv](#), 2412.16513 (2024), [arXiv:2412.16513 \[hep-ph\]](#).
- [32] P. Char and C. Mondal, Exploring the limits of nucleonic metamodelling using different relativistic density functionals, [arXiv](#), 2502.04211 (2025), [arXiv:2502.04211 \[nucl-th\]](#).
- [33] B. P. Abbott, R. Abbott, T. D. Abbott, *et al.* (LIGO Scientific, Virgo), GW170817: Observation of Gravitational Waves from a Binary Neutron Star Inspiral, *Phys. Rev. Lett.* **119**, 161101 (2017), [arXiv:1710.05832 \[gr-qc\]](#).
- [34] B. P. Abbott, R. Abbott, T. D. Abbot, *et al.* (LIGO Scien-

- tific, Virgo), GW170817: Measurements of neutron star radii and equation of state, *Phys. Rev. Lett.* **121**, 161101 (2018), [arXiv:1805.11581 \[gr-qc\]](#).
- [35] B. P. Abbott, R. Abbott, T. D. Abbot, *et al.* (LIGO Scientific, Virgo), Properties of the binary neutron star merger GW170817, *Phys. Rev. X* **9**, 011001 (2019), [arXiv:1805.11579 \[gr-qc\]](#).
- [36] B. P. Abbott, R. Abbott, T. D. Abbott, *et al.* (LIGO Scientific, Virgo), GW190425: Observation of a Compact Binary Coalescence with Total Mass $\sim 3.4M_{\odot}$, *Astrophys. J. Lett.* **892**, L3 (2020), [arXiv:2001.01761 \[astro-ph.HE\]](#).
- [37] M. C. Miller, F. K. Lamb, A. J. Dittmann, *et al.*, The Radius of PSR J0740+6620 from NICER and XMM-Newton Data, *Astrophys. J. Lett.* **918**, L28 (2021), [arXiv:2105.06979 \[astro-ph.HE\]](#).
- [38] T. E. Riley, A. L. Watts, P. S. Ray, *et al.*, A NICER View of the Massive Pulsar PSR J0740+6620 Informed by Radio Timing and XMM-Newton Spectroscopy, *Astrophys. J. Lett.* **918**, L27 (2021), [arXiv:2105.06980 \[astro-ph.HE\]](#).
- [39] T. Salmi, D. Choudhury, Y. Kini, *et al.*, The Radius of the High-mass Pulsar PSR J0740+6620 with 3.6 yr of NICER Data, *Astrophys. J.* **974**, 294 (2024), [arXiv:2406.14466 \[astro-ph.HE\]](#).
- [40] S. Vinciguerra, T. Salmi, A. L. Watts, *et al.*, An Updated Mass–Radius Analysis of the 2017–2018 NICER Data Set of PSR J0030+0451, *Astrophys. J.* **961**, 62 (2024), [arXiv:2308.09469 \[astro-ph.HE\]](#).
- [41] M. C. Miller, F. K. Lamb, A. J. Dittmann, *et al.*, PSR J0030+0451 Mass and Radius from *NICER* Data and Implications for the Properties of Neutron Star Matter, *Astrophys. J. Lett.* **887**, L24 (2019), [arXiv:1912.05705 \[astro-ph.HE\]](#).
- [42] T. E. Riley, A. L. Watts, S. Bogdanov, *et al.*, A *NICER* View of PSR J0030+0451: Millisecond Pulsar Parameter Estimation, *Astrophys. J. Lett.* **887**, L21 (2019), [arXiv:1912.05702 \[astro-ph.HE\]](#).
- [43] D. Choudhury, T. Salmi, S. Vinciguerra, *et al.*, A *NICER* View of the Nearest and Brightest Millisecond Pulsar: PSR J0437–4715, *Astrophys. J. Lett.* **971**, L20 (2024), [arXiv:2407.06789 \[astro-ph.HE\]](#).
- [44] T. Salmi, J. S. Deneva, P. S. Ray, *et al.*, A *NICER* View of PSR J1231–1411: A Complex Case, *Astrophys. J.* **976**, 58 (2024), [arXiv:2409.14923 \[astro-ph.HE\]](#).
- [45] J. J. Li, A. Sedrakian, and M. Alford, Confronting new *NICER* mass-radius measurements with phase transition in dense matter and twin compact stars, *Jour. Cosmo. Astropart. Phys.* **02**, 002 (2025), [arXiv:2409.05322 \[astro-ph.HE\]](#).
- [46] P. S. Shternin, D. D. Ofengeim, W. C. G. Ho, C. O. Heinke, M. J. P. Wijngaarden, and D. J. Patnaude, Model-independent constraints on superfluidity from the cooling neutron star in Cassiopeia A, *Mon. Not. Roy. Astron. Soc.* **506**, 709 (2021), [arXiv:2106.05692 \[astro-ph.HE\]](#).
- [47] J. J. Li, A. Sedrakian, and F. Weber, Universal relations for compact stars with heavy baryons, *Phys. Rev. C* **108**, 025810 (2023), [arXiv:2306.14190 \[nucl-th\]](#).
- [48] J. Antoniadis, P. C. C. Freire, N. Wex, *et al.*, A Massive Pulsar in a Compact Relativistic Binary, *Science* **340**, 6131 (2013), [arXiv:1304.6875 \[astro-ph.HE\]](#).
- [49] H. T. Cromartie, E. Fonseca, S. M. Ransom, *et al.* (NANOGrav), Relativistic Shapiro delay measurements of an extremely massive millisecond pulsar, *Nat. Astron.* **4**, 72 (2019), [arXiv:1904.06759 \[astro-ph.HE\]](#).
- [50] E. Fonseca, H. T. Cromartie, T. T. Pennucci, *et al.*, Refined Mass and Geometric Measurements of the High-mass PSR J0740+6620, *Astrophys. J. Lett.* **915**, L12 (2021), [arXiv:2104.00880 \[astro-ph.HE\]](#).
- [51] M. Soares-Santos, D. E. Holz, J. Annis, *et al.* (DES, Dark Energy Camera GW-EM), The Electromagnetic Counterpart of the Binary Neutron Star Merger LIGO/Virgo GW170817. I. Discovery of the Optical Counterpart Using the Dark Energy Camera, *Astrophys. J. Lett.* **848**, L16 (2017), [arXiv:1710.05459 \[astro-ph.HE\]](#).
- [52] V. A. Villar, J. Guillochon, E. Berger, *et al.*, The Combined Ultraviolet, Optical, and Near-Infrared Light Curves of the Kilonova Associated with the Binary Neutron Star Merger GW170817: Unified Data Set, Analytic Models, and Physical Implications, *Astrophys. J. Lett.* **851**, L21 (2017), [arXiv:1710.11576 \[astro-ph.HE\]](#).
- [53] M. Shibata, S. Fujibayashi, K. Hotokezaka, *et al.*, Modeling GW170817 based on numerical relativity and its implications, *Phys. Rev. D* **96**, 123012 (2017), [arXiv:1710.07579 \[astro-ph.HE\]](#).
- [54] B. Margalit and B. D. Metzger, Constraining the Maximum Mass of Neutron Stars From Multi-Messenger Observations of GW170817, *Astrophys. J. Lett.* **850**, L19 (2017), [arXiv:1710.05938 \[astro-ph.HE\]](#).
- [55] M. Ruiz, S. L. Shapiro, and A. Tsokaros, GW170817, General Relativistic Magnetohydrodynamic Simulations, and the Neutron Star Maximum Mass, *Phys. Rev. D* **97**, 021501 (2018), [arXiv:1711.00473 \[astro-ph.HE\]](#).
- [56] L. Rezzolla, E. R. Most, and L. R. Weih, Using gravitational-wave observations and quasi-universal relations to constrain the maximum mass of neutron stars, *Astrophys. J. Lett.* **852**, L25 (2018), [arXiv:1711.00314 \[astro-ph.HE\]](#).
- [57] M. Shibata, E. Zhou, K. Kiuchi, and S. Fujibayashi, Constraint on the maximum mass of neutron stars using GW170817 event, *Phys. Rev. D* **100**, 023015 (2019), [arXiv:1905.03656 \[astro-ph.HE\]](#).
- [58] S. Khadkikar, A. R. Raduta, M. Oertel, and A. Sedrakian, Maximum mass of compact stars from gravitational wave events with finite-temperature equations of state, *Phys. Rev. C* **103**, 055811 (2021), [arXiv:2102.00988 \[astro-ph.HE\]](#).
- [59] R. W. Romani, D. Kandel, A. V. Filippenko, T. G. Brink, and W. Zheng, PSR J0952–0607: The Fastest and Heaviest Known Galactic Neutron Star, *Astrophys. J. Lett.* **934**, L17 (2022), [arXiv:2207.05124 \[astro-ph.HE\]](#).
- [60] E. D. Barr, A. Dutta, P. C. C. Freire, *et al.*, A pulsar in a binary with a compact object in the mass gap between neutron stars and black holes, *Science* **383**, 275 (2024), [arXiv:2401.09872 \[astro-ph.HE\]](#).
- [61] R. Abbott, T. D. Abbott, S. Abraham, *et al.* (LIGO Scientific, Virgo), GW190814: Gravitational Waves from the Coalescence of a 23 Solar Mass Black Hole with a 2.6 Solar Mass Compact Object, *Astrophys. J. Lett.* **896**, L44 (2020), [arXiv:2006.12611 \[astro-ph.HE\]](#).
- [62] R. Abbott, T. D. Abbott, F. Acernese, *et al.* (KAGRA, VIRGO, LIGO Scientific), GWTC-3: Compact Binary Coalescences Observed by LIGO and Virgo during the Second Part of the Third Observing Run, *Phys. Rev. X* **13**, 041039 (2023), [arXiv:2111.03606 \[gr-qc\]](#).
- [63] A. G. Abac, R. Abbott, I. Abouelfettouh, *et al.* (LIGO Scientific, Virgo, KAGRA), Observation of Gravitational Waves from the Coalescence of a 2.5–4.5 M_{\odot} Compact Object and a Neutron Star, *Astrophys. J. Lett.* **970**, L34 (2024), [arXiv:2404.04248 \[astro-ph.HE\]](#).
- [64] V. Doroshenko, V. Suleimanov, G. Pühlhofer, and A. Santangelo, A strangely light neutron star within a supernova remnant, *Nat. Astron.* **6**, 1444 (2022).
- [65] J. J. Li and A. Sedrakian, Baryonic models of ultra-low-mass

- compact stars for the central compact object in HESS J1731-347, *Phys. Lett. B* **844**, 138062 (2023), [arXiv:2306.14185 \[nucl-th\]](#).
- [66] L. Brodie and A. Haber, Nuclear and hybrid equations of state in light of the low-mass compact star in HESS J1731-347, *Phys. Rev. C* **108**, 025806 (2023), [arXiv:2302.02989 \[nucl-th\]](#).
- [67] S. Kubis, W. Wójcik, D. A. Castillo, and N. Zabari, Relativistic mean-field model for the ultracompact low-mass neutron star HESS J1731-347, *Phys. Rev. C* **108**, 045803 (2023), [arXiv:2307.02979 \[nucl-th\]](#).
- [68] V. Sagun, E. Giangrandi, T. Dietrich, O. Ivanytskyi, R. Nereiros, and C. Providência, What Is the Nature of the HESS J1731-347 Compact Object?, *Astrophys. J.* **958**, 49 (2023), [arXiv:2306.12326 \[astro-ph.HE\]](#).
- [69] B. Gao, Y. Yan, and M. Harada, Reconciling constraints from the supernova remnant HESS J1731-347 with the parity doublet model, *Phys. Rev. C* **109**, 065807 (2024), [arXiv:2404.04786 \[nucl-th\]](#).
- [70] J. J. Li, A. Sedrakian, and M. Alford, Hybrid Star Models in the Light of New Multimessenger Data, *Astrophys. J.* **967**, 116 (2024), [arXiv:2401.02198 \[astro-ph.HE\]](#).
- [71] J. A. J. Alford and J. P. Halpern, Do Central Compact Objects have Carbon Atmospheres?, *Astrophys. J.* **944**, 36 (2023), [arXiv:2302.05893 \[astro-ph.HE\]](#).
- [72] Y. Kini, T. Salmi, S. Vinciguerra, *et al.*, Constraining the Properties of the Thermonuclear Burst Oscillation Source XTE J1814-338 Through Pulse Profile Modelling, *Mon. Not. Roy. Astron. Soc.* **535**, 1507 (2024), [arXiv:2405.10717 \[astro-ph.HE\]](#).
- [73] K. Hebeler, J. M. Lattimer, C. J. Pethick, and A. Schwenk, Equation of state and neutron star properties constrained by nuclear physics and observation, *Astrophys. J.* **773**, 11 (2013), [arXiv:1303.4662 \[astro-ph.SR\]](#).
- [74] J. E. Lynn, I. Tews, J. Carlson, S. Gandolfi, A. Gezerlis, K. E. Schmidt, and A. Schwenk, Chiral Three-Nucleon Interactions in Light Nuclei, Neutron- α Scattering, and Neutron Matter, *Phys. Rev. Lett.* **116**, 062501 (2016), [arXiv:1509.03470 \[nucl-th\]](#).
- [75] C. Drischler, K. Hebeler, and A. Schwenk, Chiral interactions up to next-to-next-to-next-to-leading order and nuclear saturation, *Phys. Rev. Lett.* **122**, 042501 (2019), [arXiv:1710.08220 \[nucl-th\]](#).
- [76] J. Keller, K. Hebeler, and A. Schwenk, Nuclear Equation of State for Arbitrary Proton Fraction and Temperature Based on Chiral Effective Field Theory and a Gaussian Process Emulator, *Phys. Rev. Lett.* **130**, 072701 (2023), [arXiv:2204.14016 \[nucl-th\]](#).
- [77] M. Oertel, M. Hempel, T. Klähn, and S. Typel, Equations of state for supernovae and compact stars, *Rev. Mod. Phys.* **89**, 015007 (2017), [arXiv:1610.03361 \[astro-ph.HE\]](#).
- [78] M. Grasso, Effective density functionals beyond mean field, *Prog. Part. Nucl. Phys.* **106**, 256 (2019), [arXiv:1811.01039 \[nucl-th\]](#).
- [79] J. Yang and J. Piekarewicz, Covariant Density Functional Theory in Nuclear Physics and Astrophysics, *Ann. Rev. Nucl. Part. Sci.* **70**, 21 (2020), [arXiv:1912.11112 \[nucl-th\]](#).
- [80] A. Sedrakian, J. J. Li, and F. Weber, Heavy baryons in compact stars, *Prog. Part. Nucl. Phys.* **131**, 104041 (2023), [arXiv:2212.01086 \[nucl-th\]](#).
- [81] J. Margueron, R. Hoffmann Casali, and F. Gulminelli, Equation of state for dense nucleonic matter from metamodelling. II. Predictions for neutron star properties, *Phys. Rev. C* **97**, 025806 (2018), [arXiv:1708.06895 \[nucl-th\]](#).
- [82] N.-B. Zhang and B.-A. Li, GW190814's Secondary Component with Mass 2.50–2.67 M_{\odot} as a Superfast Pulsar, *Astrophys. J.* **902**, 38 (2020), [arXiv:2007.02513 \[astro-ph.HE\]](#).
- [83] S. Huth, P. T. H. Pang, I. Tews, *et al.*, Constraining Neutron-Star Matter with Microscopic and Macroscopic Collisions, *Nature* **606**, 276 (2022), [arXiv:2107.06229 \[nucl-th\]](#).
- [84] N. Yao, A. Sorensen, V. Dexheimer, and J. Noronha-Hostler, Structure in the speed of sound: From neutron stars to heavy-ion collisions, *Phys. Rev. C* **109**, 065803 (2024), [arXiv:2311.18819 \[nucl-th\]](#).
- [85] E. Annala, T. Gorda, A. Kurkela, and A. Vuorinen, Gravitational-wave constraints on the neutron-star-matter Equation of State, *Phys. Rev. Lett.* **120**, 172703 (2018), [arXiv:1711.02644 \[astro-ph.HE\]](#).
- [86] D. Vretenar, A. V. Afanasjev, G. A. Lalazissis, and P. Ring, Relativistic Hartree Bogoliubov theory: static and dynamic aspects of exotic nuclear structure, *Phys. Rept.* **409**, 101 (2005).
- [87] T. Niksic, D. Vretenar, and P. Ring, Relativistic Nuclear Energy Density Functionals: Mean-Field and Beyond, *Prog. Part. Nucl. Phys.* **66**, 519 (2011), [arXiv:1102.4193 \[nucl-th\]](#).
- [88] S. Typel and H. H. Wolter, Relativistic mean field calculations with density dependent meson nucleon coupling, *Nucl. Phys. A* **656**, 331 (1999).
- [89] G. A. Lalazissis, T. Niksic, D. Vretenar, and P. Ring, New relativistic mean-field interaction with density-dependent meson-nucleon couplings, *Phys. Rev. C* **71**, 024312 (2005).
- [90] J. J. Li and A. Sedrakian, New Covariant Density Functionals of Nuclear Matter for Compact Star Simulations, *Astrophys. J.* **957**, 41 (2023), [arXiv:2308.14457 \[nucl-th\]](#).
- [91] J. D. Walecka, A Theory of highly condensed matter, *Ann. Phys.* **83**, 491 (1974).
- [92] P. G. Reinhard, The Relativistic Mean Field Description of Nuclei and Nuclear Dynamics, *Rept. Prog. Phys.* **52**, 439 (1989).
- [93] J. J. Li, W. H. Long, and A. Sedrakian, Hypernuclear stars from relativistic Hartree-Fock density functional theory, *Eur. Phys. J. A* **54**, 133 (2018), [arXiv:1801.07084 \[nucl-th\]](#).
- [94] J. J. Li, W. H. Long, J. Margueron, and N. Van Giai, Superheavy magic structures in the relativistic Hartree-Fock-Bogoliubov approach, *Phys. Lett. B* **732**, 169 (2014), [arXiv:1303.2765 \[nucl-th\]](#).
- [95] J. J. Li and A. Sedrakian, Constraining compact star properties with nuclear saturation parameters, *Phys. Rev. C* **100**, 015809 (2019), [arXiv:1903.06057 \[astro-ph.HE\]](#).
- [96] J. J. Li and A. Sedrakian, Implications from GW170817 for Δ -isobar Admixed Hypernuclear Compact Stars, *Astrophys. J. Lett.* **874**, L22 (2019), [arXiv:1904.02006 \[nucl-th\]](#).
- [97] G. Baym, C. Pethick, and P. Sutherland, The ground state of matter at high densities: equation of state and stellar models, *Astrophys. J.* **170**, 299 (1971).
- [98] G. Baym, H. A. Bethe, and C. J. Pethick, Neutron star matter, *Nucl. Phys. A* **175**, 225 (1971).
- [99] R. C. Tolman, Static solutions of Einstein's field equations for spheres of fluid, *Phys. Rev.* **55**, 364 (1939).
- [100] J. R. Oppenheimer and G. M. Volkoff, On massive neutron cores, *Phys. Rev.* **55**, 374 (1939).
- [101] E. E. Flanagan and T. Hinderer, Constraining neutron star tidal Love numbers with gravitational wave detectors, *Phys. Rev. D* **77**, 021502 (2008), [arXiv:0709.1915 \[astro-ph\]](#).
- [102] T. Hinderer, Tidal Love numbers of neutron stars, *Astrophys. J.* **677**, 1216 (2008), [arXiv:0711.2420 \[astro-ph\]](#).
- [103] F. Feroz, M. P. Hobson, and M. Bridges, MultiNest: an efficient and robust Bayesian inference tool for cosmology and particle physics, *Mon. Not. Roy. Astron. Soc.* **398**, 1601 (2009), [arXiv:0809.3437 \[astro-ph\]](#).

- [104] J. Buchner, A. Georgakakis, K. Nandra, L. Hsu, C. Rangel, M. Brightman, A. Merloni, M. Salvato, J. Donley, and D. Kocevski, X-ray spectral modelling of the AGN obscuring region in the CDFS: Bayesian model selection and catalogue, *Astron. Astrophys.* **564**, A125 (2014), arXiv:1402.0004 [astro-ph.HE].
- [105] F. Ferroz, M. P. Hobson, E. Cameron, and A. N. Pettitt, Importance Nested Sampling and the MultiNest Algorithm, *Open J. Astrophys.* **2**, 10 (2019), arXiv:1306.2144 [astro-ph.IM].
- [106] D. Adhikari, H. Albataineh, D. Androic, *et al.* (PREX), Accurate Determination of the Neutron Skin Thickness of ^{208}Pb through Parity-Violation in Electron Scattering, *Phys. Rev. Lett.* **126**, 172502 (2021), arXiv:2102.10767 [nucl-ex].
- [107] D. Adhikari, H. Albataineh, D. Androic, *et al.* (CREX), Precision Determination of the Neutral Weak Form Factor of Ca48, *Phys. Rev. Lett.* **129**, 042501 (2022), arXiv:2205.11593 [nucl-ex].
- [108] B. T. Reed, F. J. Fattoyev, C. J. Horowitz, and J. Piekarewicz, Implications of PREX-2 on the Equation of State of Neutron-Rich Matter, *Phys. Rev. Lett.* **126**, 172503 (2021), arXiv:2101.03193 [nucl-th].
- [109] P.-G. Reinhard, X. Roca-Maza, and W. Nazarewicz, Information Content of the Parity-Violating Asymmetry in Pb208, *Phys. Rev. Lett.* **127**, 232501 (2021), arXiv:2105.15050 [nucl-th].
- [110] M. Dutra, O. Lourenço, S. S. Avancini, B. V. Carlson, A. Delfino, D. P. Menezes, C. Providência, S. Typel, and J. R. Stone, Relativistic Mean-Field Hadronic Models under Nuclear Matter Constraints, *Phys. Rev. C* **90**, 055203 (2014), arXiv:1405.3633 [nucl-th].
- [111] C. Kalapotharakos, Z. Wadiasingh, A. K. Harding, and D. Kazanas, The Multipolar Magnetic Field of Millisecond Pulsar PSR J0030+0451, *Astrophys. J.* **907**, 63 (2021), arXiv:2009.08567 [astro-ph.HE].
- [112] F. Hernandez Vivanco, R. Smith, E. Thrane, and P. D. Lasky, A scalable random forest regressor for combining neutron-star equation of state measurements: A case study with GW170817 and GW190425, *Mon. Not. R. Astron. Soc.* **499**, 5972 (2020), arXiv:2008.05627 [astro-ph.HE].
- [113] C. Drischler, S. Han, J. M. Lattimer, M. Prakash, S. Reddy, and T. Zhao, Limiting masses and radii of neutron stars and their implications, *Phys. Rev. C* **103**, 045808 (2021), arXiv:2009.06441 [nucl-th].
- [114] D. Klahn, T. Blaschke, S. Typel, *et al.*, Constraints on the high-density nuclear equation of state from the phenomenology of compact stars and heavy-ion collisions, *Phys. Rev. C* **74**, 035802 (2006), arXiv:nucl-th/0602038.
- [115] A. Sedrakian, Short-Range Correlations and Urca Process in Neutron Stars, *Phys. Rev. Lett.* **133**, 171401 (2024), arXiv:2406.16183 [nucl-th].
- [116] J. J. Li, A. Sedrakian, and F. Weber, Competition between delta isobars and hyperons and properties of compact stars, *Phys. Lett. B* **783**, 234 (2018), arXiv:1803.03661 [nucl-th].
- [117] M. Fortin, A. R. Raduta, S. Avancini, and C. Providência, Thermal evolution of relativistic hyperonic compact stars with calibrated equations of state, *Phys. Rev. D* **103**, 083004 (2021), arXiv:2102.07565 [nucl-th].
- [118] P. Danielewicz, R. Lacey, and W. G. Lynch, Determination of the equation of state of dense matter, *Science* **298**, 1592 (2002), arXiv:nucl-th/0208016.
- [119] C. Fuchs, Strangeness production in heavy ion reactions at intermediate-energies, *Prog. Part. Nucl. Phys.* **53**, 113 (2004), arXiv:nucl-th/0312052.
- [120] W. G. Lynch, M. B. Tsang, Y. Zhang, P. Danielewicz, M. Famiano, Z. Li, and A. W. Steiner, Probing the Symmetry Energy with Heavy Ions, *Prog. Part. Nucl. Phys.* **62**, 427 (2009), arXiv:0901.0412 [nucl-ex].
- [121] A. Le Fèvre, Y. Leifels, W. Reisdorf, J. Aichelin, and C. Hartnack, Constraining the nuclear matter equation of state around twice saturation density, *Nucl. Phys. A* **945**, 112 (2016), arXiv:1501.05246 [nucl-ex].
- [122] M. B. Tsang, Y. Zhang, P. Danielewicz, M. Famiano, Z. Li, W. G. Lynch, and A. W. Steiner, Constraints on the density dependence of the symmetry energy, *Phys. Rev. Lett.* **102**, 122701 (2009), arXiv:0811.3107 [nucl-ex].
- [123] P. Russotto, P. Z. Wu, M. Zoric, *et al.*, Symmetry energy from elliptic flow in $^{197}\text{Au} + ^{197}\text{Au}$, *Phys. Lett. B* **697**, 471 (2011), arXiv:1101.2361 [nucl-ex].
- [124] P. Russotto, S. Gannon, S. Kupnyothers, *et al.*, Results of the ASY-EOS experiment at GSI: The symmetry energy at suprasaturation density, *Phys. Rev. C* **94**, 034608 (2016), arXiv:1608.04332 [nucl-ex].
- [125] P. Danielewicz and J. Lee, Symmetry Energy II: Isobaric Analog States, *Nucl. Phys. A* **922**, 1 (2014), arXiv:1307.4130 [nucl-th].
- [126] W. G. Lynch and M. B. Tsang, Decoding the density dependence of the nuclear symmetry energy, *Phys. Lett. B* **830**, 137098 (2022), arXiv:2106.10119 [nucl-th].
- [127] C. Musolino, C. Ecker, and L. Rezzolla, On the Maximum Mass and Oblateness of Rotating Neutron Stars with Generic Equations of State, *Astrophys. J.* **962**, 61 (2024), arXiv:2307.03225 [gr-qc].
- [128] C. J. Horowitz and J. Piekarewicz, Neutron star structure and the neutron radius of Pb-208, *Phys. Rev. Lett.* **86**, 5647 (2001), arXiv:astro-ph/0010227.
- [129] F. J. Fattoyev, J. Carvajal, W. G. Newton, and B.-A. Li, Constraining the high-density behavior of the nuclear symmetry energy with the tidal polarizability of neutron stars, *Phys. Rev. C* **87**, 015806 (2013), arXiv:1210.3402 [nucl-th].
- [130] M. Fortin, C. Providencia, A. R. Raduta, F. Gulminelli, J. L. Zdunik, P. Haensel, and M. Bejger, Neutron star radii and crusts: uncertainties and unified equations of state, *Phys. Rev. C* **94**, 035804 (2016), arXiv:1604.01944 [astro-ph.SR].
- [131] N. Hornick, L. Tolos, A. Zacchi, J.-E. Christian, and J. Schaffner-Bielich, Relativistic parameterizations of neutron matter and implications for neutron stars, *Phys. Rev. C* **98**, 065804 (2018), arXiv:1808.06808 [astro-ph.HE].